Received: 2024-06-18 | Accepted: 2024-09-07 | Published: 2024-12-20

Looking for Ancient Metalworking Sites of Luristan (Western Iran): a Preliminary Archaeometallurgical Approach

Zahra Hashemi, Nima Nezafati and Daniel Demant

Keywords
Iron working, smelting slag, smithing slag, geochemistry, mineralogy, lead isotope analysis, rare earth elements (REE)

Abstract

The region of Luristan in the Zagros Mountains (western Iran) is known worldwide for its skilled and enigmatic ancient metal production, in particular its "Luristan Bronzes" dated to the Bronze and Iron Ages. At the crossroads between the IInd and Ist millennia BC, in parallel with tradition of elaborate bronze production, Luristan also saw the arrival of iron. Bimetallic bronze-iron artefacts and technically well-developed iron mask swords are among very notable iron products of Luristan metalworkers and are potentially among the oldest iron artefacts known from Iran. Despite this situation, technical aspects of iron metallurgy are almost unknown in Luristan. Field investigations are rare, archaeological production contexts are unknown, and little attention has been paid to iron metalworking. This article, as an initial step in this field, will address the results of a recent short archaeometallurgical survey in Luristan which lead to the discovery of five slag heaps. The physicochemical analyses and microscopic observations, which were carried out at the Departments of Mining Archaeology and Archaeometallurgy of the German Mining Museum, Bochum (DBM), Germany, indicated that we have identified several ironworking workshops: mostly smelting together with some vestiges of smithing activities. In addition, geochemical and isotopic analyses attested that the ores probably came from geochemically similar deposits in the wider region.

Introduction

Luristan Bronzes are among the most enigmatic metal artefacts known in Western Asian archaeology. They are closely associated with the Luristan region, located in the mountainous area of central Zagros (western Iran) and date from the 3rd to 1st millennia BC. They demonstrate a great morphological diversity and a very elaborate and original iconography. They arrived *en masse* in western art markets and museums, beginning in the 1930s mostly from looting for the antiquities market, but also from a handful of archaeological excavations. Soon after, they became a significant cultural marker of Luristan. In contrary to what their name suggests, they comprise not only bronze artefacts but also, fewer in numbers, iron and silver artefacts. A significant number of Luristan Bronzes are bimetallic. Alongside these, at the crossroad of the 2nd and 1st millennia BC, Luristan witnessed the appearance of the so-called iron mask swords. The production techniques of such artifacts are very intriguing. Metallographic and radiographic analyses on several of these swords show the use of techniques more appropriate to the skills of the bronze smith than those of the blacksmith (France-Lanord, 1969; Smith, 1971). Radiocarbon analysis of certain of these swords dates them to the end of the 2nd millennium BC (Rehder, 1991, pp.13-14).

Unfortunately, despite decades of archaeological research on Luristan metal artefacts, which almost exclusively come from cemeteries and sanctuaries (votive contexts), technical aspects of these objects, have remained almost unknown. Few metallurgical remains have begun to be studied by archaeometallurgists (see below) and even less attention is paid to the iron metalworking. This article is a very small window toward the unknown metalworking world of Luristan and an introduction to the iron archaeometallurgy of this region. The main purpose is to present the preliminary results of an archaeometallurgical study of slags from a recent survey in Luristan and to show the critical importance of the subject and paucity of our knowledge in this regard.

DOI:10.46586/metalla.v28.2024.i2.67-98
Licensed under Creative Commons License CC-BY 4.0.

Research history and questions

At the moment, little is known about the ancient mines and metal workshops in Luristan. The main question is, if these objects were produced in Luristan or were they imported from other regions.

From a general point of view, western Asia is rich in iron resources including both large and small deposits around which iron technology was locally developed and used intermittently across a vast territory by the last quarter of the second millennium BC (Erb-Satullo, 2019). Western Iran and Zagros Mountains, together with the Sanandaj-Sirjan metallogenic belt have an important and rich mineral position in the region (Nabatian, et al., 2015). From a geographic point of view, the Zagros Mountains are also in a strategically important location for ancient trade networks, linking Central Asia and the Indus Valley with the Caucasus, Anatolia, and Mesopotamia. These suggest a particular position for Zagros in the possible florescence of iron during the Iron Age. But where were the mines that supplied the raw materials and where are the workshops located? Who were these metalworkers?

The transition from the predominant use of copper and bronze to the simultaneous use of copper and iron in the Zagros region marks the end of the second millennium and the beginning of the first millennium BC. The excavations conducted by Holmes expedition in Sorkh Dum-I Lori (Schmidt, Van Loon and Curvers, 1989) and the French expedition in Tepe Giyan (Contenau and Ghirshman, 1935), both during 1930s, the Belgian archaeological mission in Posht Kuh (1970s) (Overlaet, 2003; Haerinck and Overlaet, 1998; 1999; 2004) as well as Iranian excavation in Sangtarashan during 2000s (Hashemi, Malekzadeh and Hasanpour, 2023), all in all attest that in the last centuries of IInd millennium BC (Iron Age I), iron jewelry appeared in Luristan. Later, at the beginning of 1st millennium BC (Iron Age II), iron started to be used for working parts of weapon blades and pin stems. Bronze remained used for handles and other more decorative parts. Around VIII-VII century BC (Iron Age III), most of the weapons and tools were made of iron, although jewelry returned to bronze.

From a technical point of view, it can be supposed that at the beginning, iron was seen as a rare luxury material used mostly for precious artefacts such as jewelry. Gradually, when its functional advantages were revealed, it started to be used for working parts of weapons. Although because of technical issues, other parts of artefacts, with elaborated decorations remained in bronze, as forming decorations with molded bronze was easier than forging iron. By mastering iron technology in Iron Age III, the majority of tools and weapons were made in iron and bronze regained its place for precious artefacts. Another suggestion which can be proposed is regarding accessibility of iron: at the end of IInd millennium BC until the middle of 1st millennium BC, iron ore became gradually accessible for the inhabitants of Luristan. As we can see, these phenomena could be a complex process, linked to specific political, technical or socio-economic situations which are obscure to this day.

Early iron mines have not been found, and evidence for the smelting and smithing of iron in the early Iron Age in Western Asia has also proven to be elusive (Pigott, 1989, p.69). With regard to archaeometallurgical analyses, they have not only been rare, but also, if conducted, were performed with particular attention mostly to the presence of carburization and techniques of heat treatment in the final artifacts. But it should be noted that a significant issue in understanding the social context of metal production lies with the workshop contexts. However, research in this area in the Luristan region suffers seriously from a lack of archaeometallurgical studies, systematic survey, and field investigation.

Among the rare vestiges concerning iron production in Luristan, as previously reported in archaeological excavations, the Holmes Expedition (1930s) can be mentioned as indicating, very briefly, the presence of iron fragments, furnace, and iron slags at Kamtarlan I, an Iron Age III settlement in Luristan (Schmidt, Van Loon and Curvers, 1989, p.5). As we don't have further information, interpretations are limited.

In addition, two archaeological surveys in Luristan have revealed several slag heaps. A field survey in the southern part of Kuh Dasht, around Botkhaneh cave identified sixteen slag heaps, the remains of iron smelting; here iron was primarily obtained from carbonate and volcanic-sedimentary rocks (Emami, Elikay Dehno and Geravand, 2017, p.90, Fig.6). The second survey between 2014 and 2019, again around the Kuh Dasht Plain, reported several slag heaps which indicate extensive iron production activity in the area (Elikay, et al., 2022). In this case, the authors (ibid. p.88) have attributed the sites to a long time span from ca. 1500 BC to the Sassanid period, although without presenting any clear dating method.

Recently, an analytical study was carried out on metallic artefacts from the Saruq Al-Hadid, an Iron Age site in the northeastern part of the Arabian Peninsula (Dubai). The geochemical similarities between the Saruq Al-Hadid iron artefacts and some contemporary Luristan artefacts from Posht-e Kuh cemeteries (from Belgian Archaeological Mission in Iran) as well as some

Figure 1. Map of Luristan region presenting the location of slag heaps, nearby archaeological sites and iron ore deposits and occurrences.

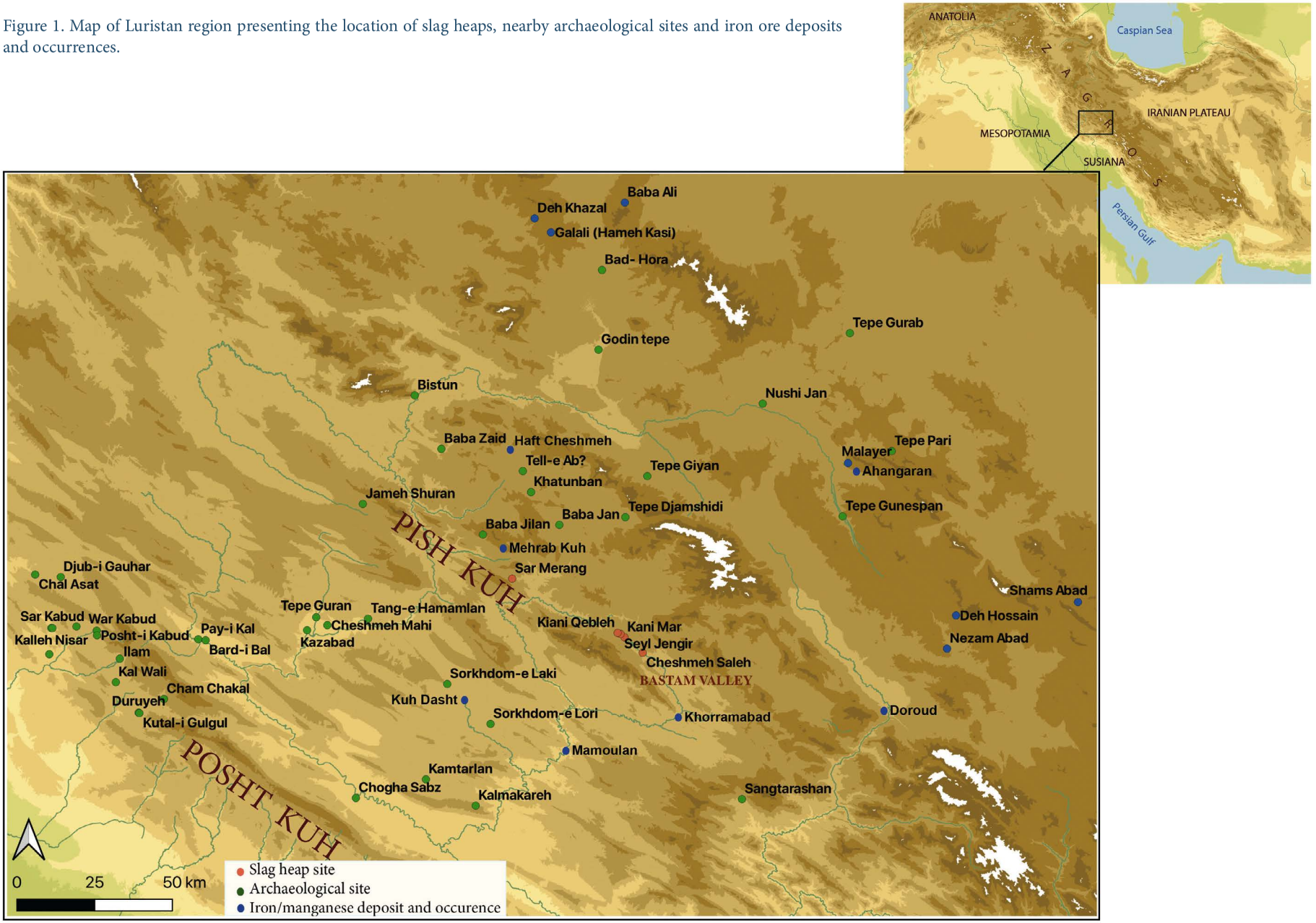

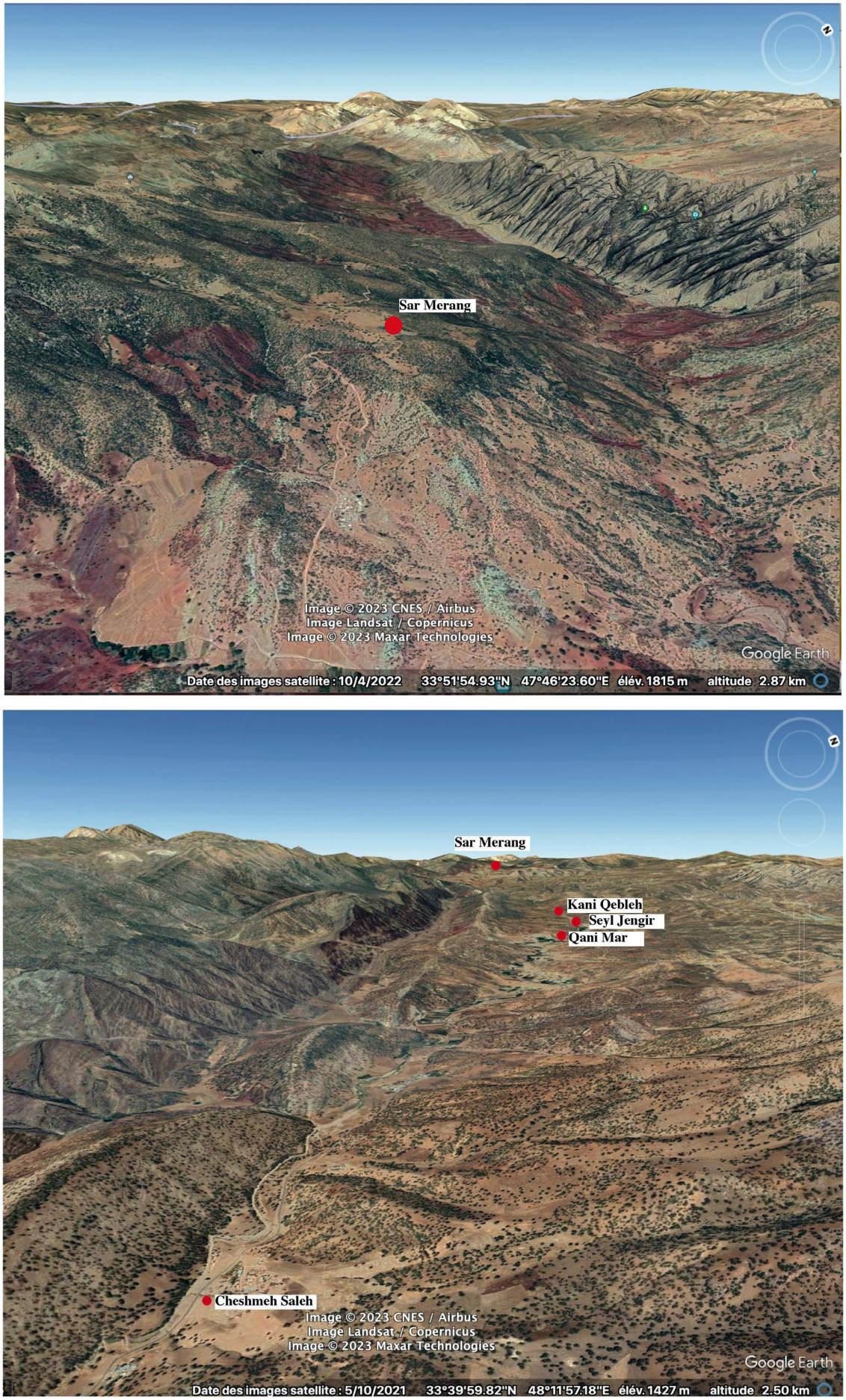

Figure 2. Location of sites in their surroundings.

ores from the Sanandaj-Sirjan metallogenic belt, led researchers to propose that these artefacts were probably imported from Luristan into the Arabian Peninsula in the form of finished products (Stepanov, et al., 2020).

In order to find out and clarify the situation of iron production organization in Luristan and to identify the location of workshops and trade networks, a systematic archaeometallurgical survey is indispensable. In this regard, during a short survey mission, in autumn 2021, five slag heaps in Luristan were visited: four in the Bastam Valley and one at Sar Merang (Figure 1). The situation did not allow for a serious methodical survey, but sites were registered and some slag pieces were collected.

In this article we deal with fifteen slag samples coming from these five archaeological sites surveyed in Luristan. Ten of them were subjected to trace elemental and isotopic analyses carried out in the German Mining Museum, Bochum.

Description of the sites

The Central Zagros and the Luristan cultural region (including the Luristan province, as well as parts of Ilam, Hamedan, and Kermanshah provinces) are composed of both large inter-mountainous valleys and high pasturelands, rich in water and forest resources. All five sites in this study are located in present-day Luristan. Four of them (Cheshmeh Saleh, Seyl Jengir, Kani Mar, and Kani Qebleh) are located in the Bastam Valley alongside a seasonal river at the east of Kamar Siah Mountain, with an altitude between 1400 and 1500 m above sea level. Sar Merang, the fifth site, is located between Mehrab Kuh to the north and Mangani Kuh to the south, on a plateau of 1820 m above sea level (Figure 2). Slag Concentration varies from one site to another. Sar Merang has the highest concentration. Slags are less densely scattered over the four other sites in Bastam Valley. Almost all of slags in all five sites are only fragments. Unfortunately, we only have a few sherds from the sites, and none of them were really diagnostic.

Cheshmeh Saleh (N 33° 39.291'; E 048° 13.220') is located at the south-east of Cheshmeh Saleh village and north of the Bastam seasonal river on a light slope at 1400 m altitude above sea level. Slag pieces are scattered on a surface of 100 x 100 m^2. On average, around 4 slag pieces can be found per 1m^2. Dimensions of the slags vary between 10 x 10 cm^2 and 3 x 3 cm^2. Some pottery sherds are scattered on the whole surface. The remains of a stone structure are visible at the north-eastern flank of the site (Figure 3).

Kani Mar (N 33° 41.950'; E 048° 09.473') is located at 8 km north-west of Cheshmeh Saleh, to the north of Sarab Chenar village, at 1520 m above sea level. Slag pieces and pottery sherds are scattered loosely on a surface of 150 x 120 m^2. On average, around 4 slag pieces can be found per 1 m^2. The dimensions of slags vary between 3 x 3 cm^2 and 5 x 5 cm^2. There are more pottery sherds than at Cheshmeh Saleh. In addition, at the upper part of the site, toward the west, fragments of a potential furnace were identified. A water spring lies in the middle of the site (Figure 4).

Seyl Jengir (N 33° 42.526'; E048° 08.664') is located at 2 km north-west of Kani Mar, to the west of Sarab Sagha village, at 1540 m above sea level. Slags are not numerous and are scattered on a surface of 50 x 50 m^2. Average dimensions of slags are 5 x 5 cm^2. Some fragments of a potential furnace wall were identified. Unfortunately, modern constructions are ongoing on the site (Figure 5).

Kani Qebleh (N 33° 42.712'; E 048° 08.040') located 1 km west of Seyl Jengir, between the modern road to the north and the river to the south, at 1560 m above sea level. Slags are scattered on a surface of 100 x 50 m^2 where their dimension varies between 3 x 3 cm^2 and 15 x 10 cm^2. Several fragments of a furnace wall have been identified. Some pottery sherds are also visible on the surface of the site. Near the river, cut by water flow, the section shows a black layer of slags in contact with a solid clay layer (Figure 6).

Sar Merang (N 33° 52.015'; E 047° 46.291') is the last site of this study, located at a higher altitude at 1820 m above sea level, on a plateau, between Mehrab Kuh to the north and Mangani Kuh to the south, relatively far from the river compared to the other sites. Slags are bigger and more densely cover the surface of the site. Around 30 slag pieces could be found per 1 m^2. On average, the dimensions of slag pieces are 10 x 10 cm^2. The slag heap of 40 x 40 m^2 seems to be part of a larger archaeological site of 70 x 100 m^2. Several architectural structures are also visible (Figure 7).

Materials and methods

Various methods were used for the scientific investigation of the samples. After a macroscopic examination, polished thin sections were produced for microscopic examination. At the same time, samples were taken from the slags to be analyzed for their mineralogical and

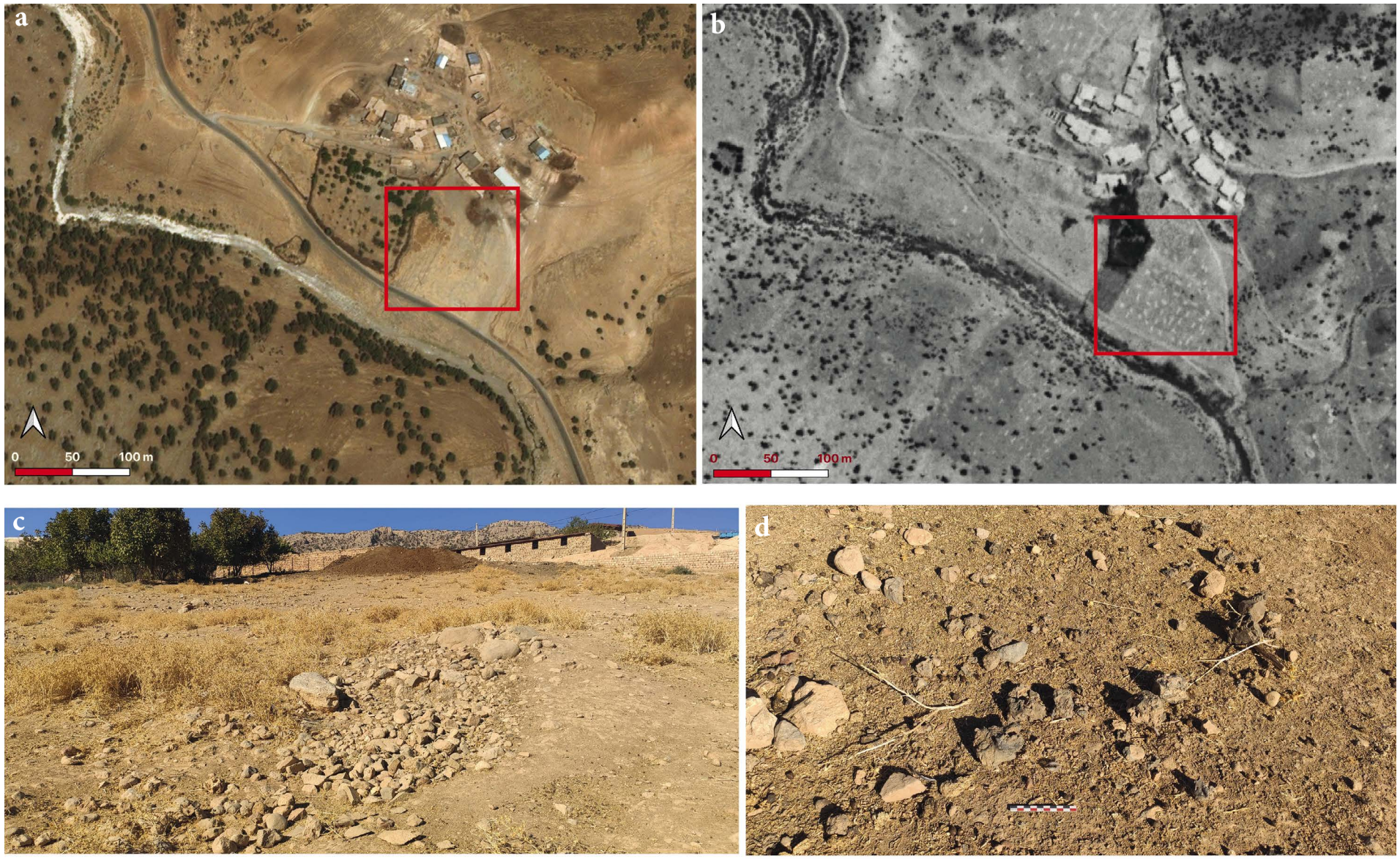

Figure 3. Cheshmeh Saleh: a. Aerial view of the site; b. Corona image of the site; c. Stone structure seen from the south-east; d. Density and average dimension of slags on the surface of the site. Photos: Z. Hashemi.

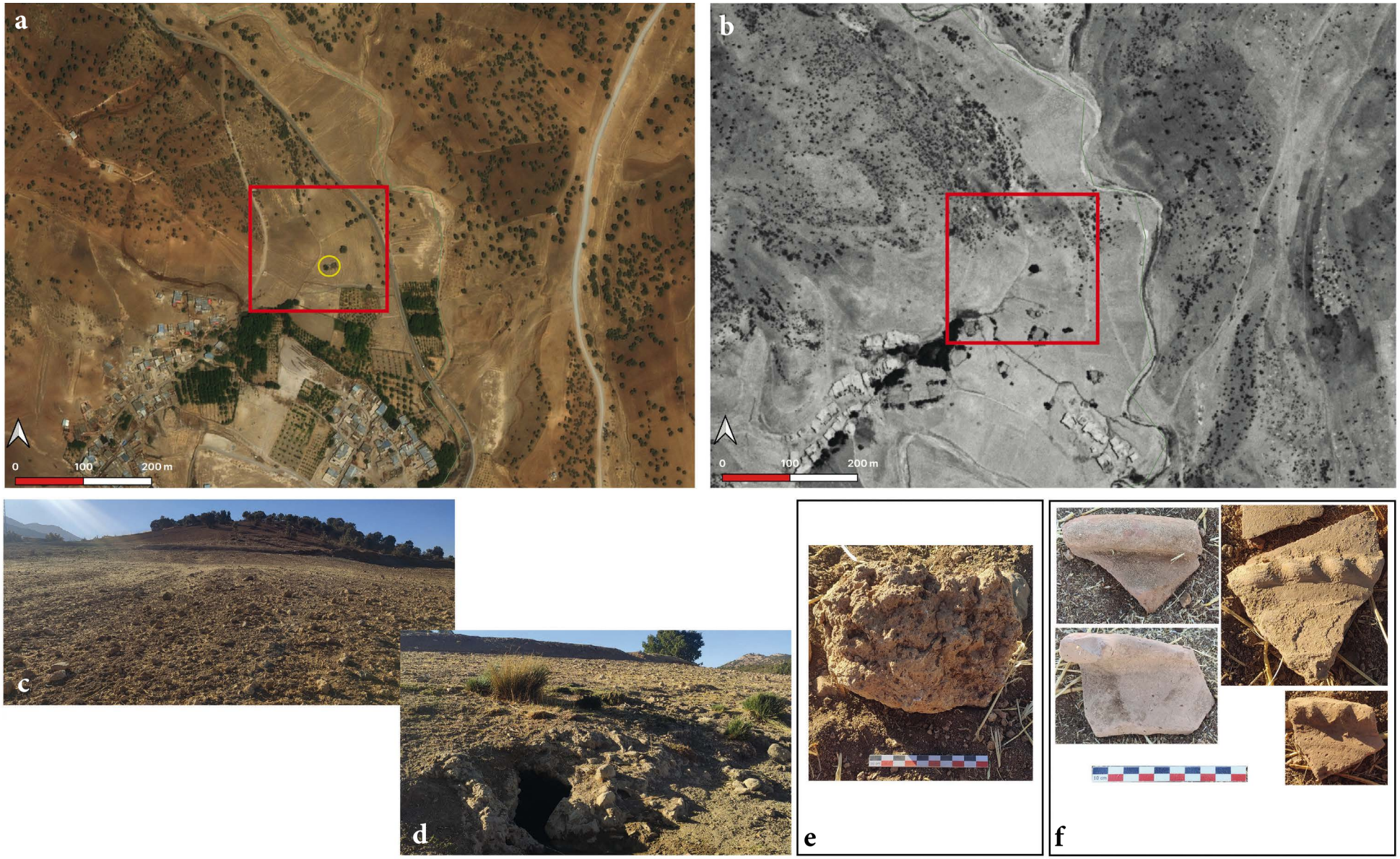

Figure 4. Kani Mar: a. Aerial view of the site with the location of the spring; b. Corona image of the site; c. General view of the site as seen from the east; d. Spring seen from the south; e. Part of a furnace wall; f. Pottery sherds on the surface of the site. Photos: Z. Hashemi.

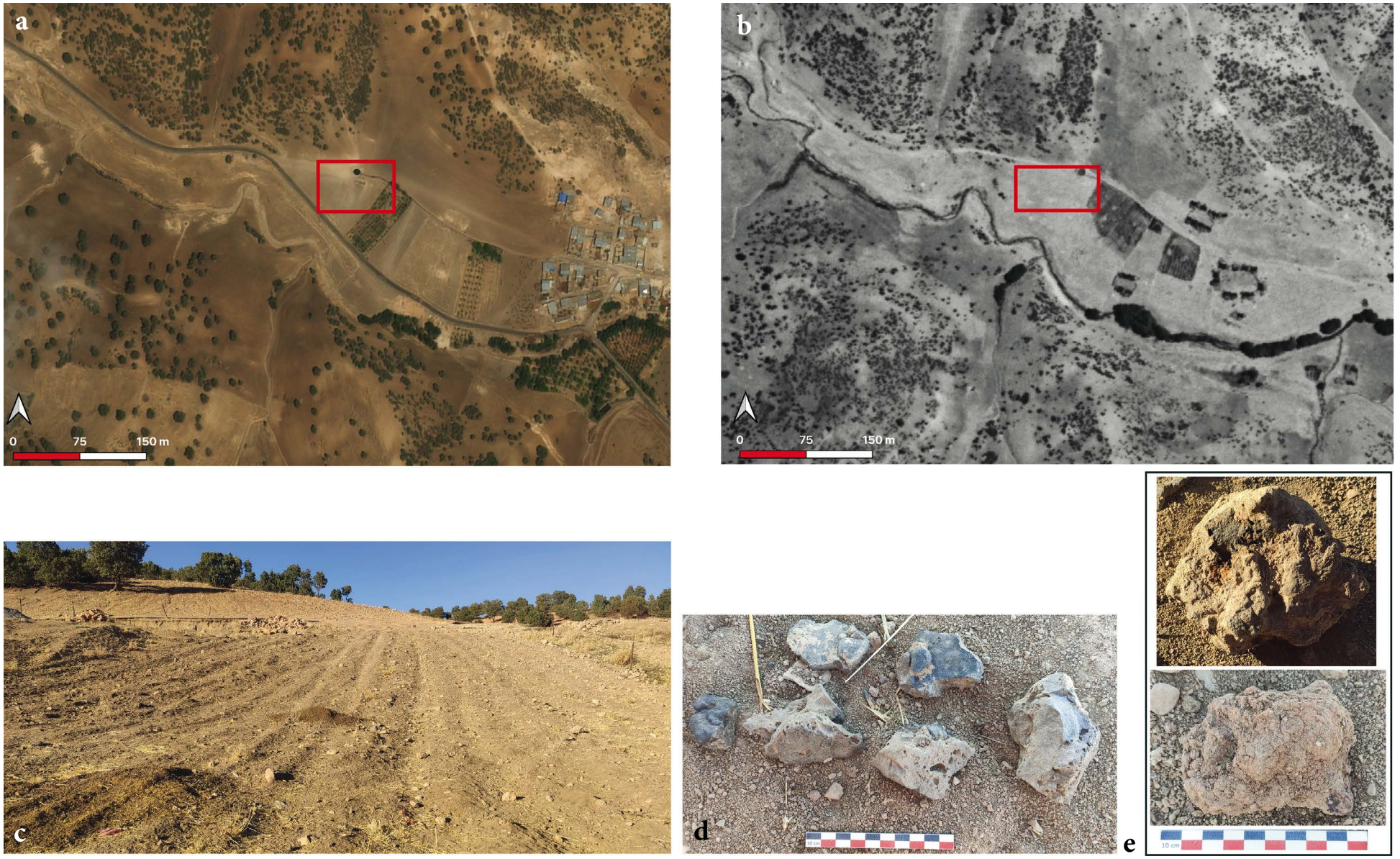

Figure 5. Seyl Jengir: a. Aerial view of the site; b. Corona image of the site; c. General view of the site, seen from the south; d. Slags scattered on the site; e. Fragments of furnace wall. Photos: Z. Hashemi.

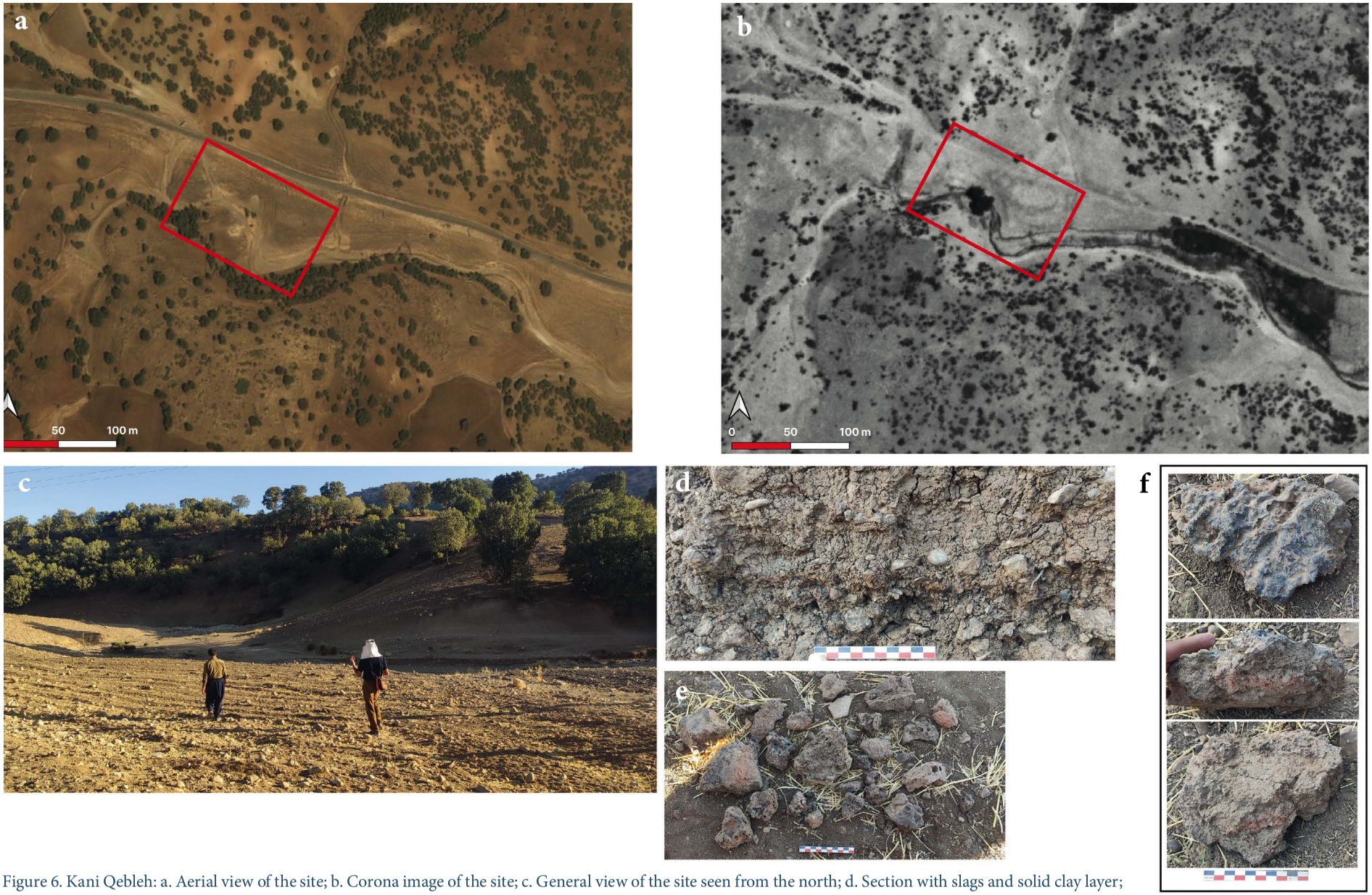

Figure 6. Kani Qebleh: a. Aerial view of the site; b. Corona image of the site; c. General view of the site seen from the north; d. Section with slags and solid clay layer; e. Slags and fragments of furnace wall on the surface of the site; f. Fragments of furnace wall. Photos: Z. Hashemi.

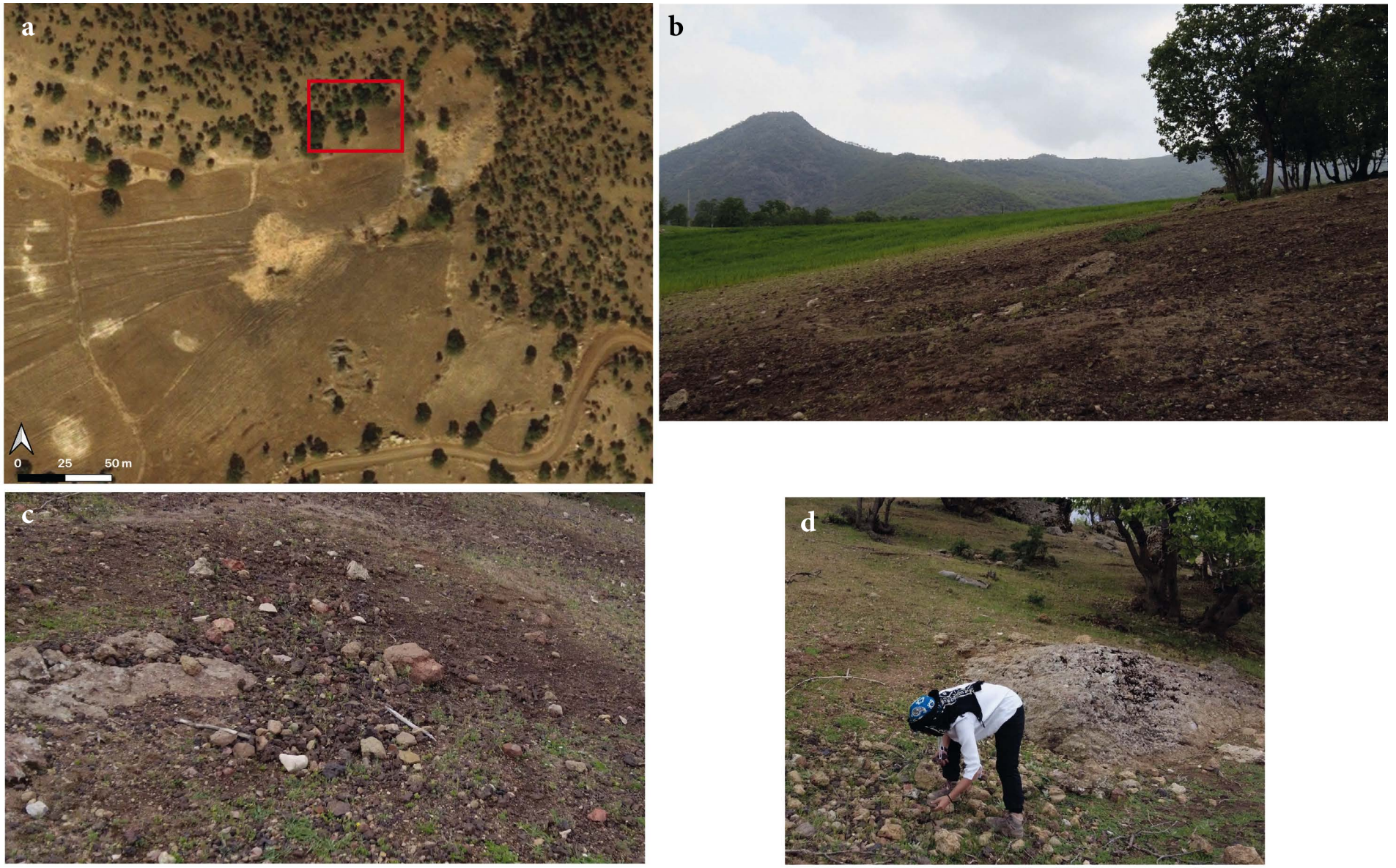

Figure 7. Sar Merang: a. Aerial view of the site; b. General view of the site seen from the north; c. Density of slags on the surface of the site; d. Slags scattered on the surface of the site and the architectural structure at the background. Photos: Z. Hashemi.

chemical composition. The samples were then ground and homogenized before being analyzed.

A polarizing microscope (Axiophot) from Zeiss was used for the structural analysis of the polished thin sections. The photographic images were taken with a Zeiss digital camera (type Axiocam 512 color) connected to the microscope and evaluated with the ZEN 2 Core program, also from Zeiss. In addition, the polished thin sections were examined using a field emission scanning electron microscope (SUPRA 40 VP, Zeiss) with a Schottky-Emitter, to which a Noran System 7 energy-dispersive X-ray spectrometer from Thermo with SDD detector is mounted. The images were recorded using a BSE detector with an acceleration voltage of 15-20 kV. For the EDS analyses an acceleration voltage of 20 kV was. The measured elements were identified using the Kα-lines. The crystalline structure analysis was carried out using an X-ray diffractometer type X` PERT Pro from PANalytical. For this, Cu Kα radiation at 45 kV and 40 mA was used. The modular device settings were selected as follows: Anti-scatter slit's (1/4°), Divergence slit (1/8°), Measuring range (5-70° 2Theta), Measuring speed (0.0167 step, 20 sec/step).

A high-resolution, double-focusing mass spectrometer from Thermo Fisher Scientific (Finnigan ELEMENT 2/XR) with inductively coupled plasma (SC-ICP-MS) was used for the chemical elemental analysis. The lead isotopes were analysed using another mass spectrometer, the Neptune XT Multi-Collector (MC-ICP-MS), also from Thermo Fisher Scientific.

For the chemistry of the slags, the sample digestion of the powdered slags were carried out with a µPREP-A microwave (MLS GmbH) after heating the powdered samples to dryness for 8 hours at 105°C. About 100 mg sample material were mixed with 1,2 g HF and 5 g HNO_3 and 5 g HCl, all concentrated, and then digested in PTFE pressure vessels for 40 min. at 250°C. In a second step, to avoid precipitation of CaF_2, FeF_3 and/or AlF_3, 10 ml of 5 % H_3BO_3 was added and the solution again was heated up for 20 min. Finally, the digested samples were diluted with ultra-pure water up to 100 ml for a concentration of about 1000 mg/L. The Quantification was done with external calibration. For main and minor elements, sample solutions were diluted 1:100, for traces 1:10 with 5% HNO_3. 1ppb In was added as an internal standard. The analyses were carried out with a FAST SC-system, ST 5532 PFA µ-FLOW nebulizer, Peltier-cooled PFA spray chamber and 1.8 mm sapphire injector in triple detector mode at all three different mass resolutions (m/Δm) depending on the elements of interest. Measurements were controlled with matrix-compatible standard material GBW07107/GSR-5, LGC Standards, Teddington, Middlesex, UK) and FER-1 and FER-2 (Canadian Certified Reference Materials Project). Relative standard deviation (RSD) for trace elements varied between 1 and 15 % (REE), for main and minor elements between 0.5 and 3 %.

To determine the lead isotope ratios, the Pb isotopes were measured using wet plasma conditions. Following classical HBr based ion exchange chromatography (AG1-X8 resin, Bio-Rad Laboratories, Inc.), 200 ppb lead solutions were doped with 50 ppb thallium (NIST SRM 997) for mass bias correction. ^{202}Hg was recorded for interference correction. The reference material NIST SRM 981 was measured in the same way to compensate drift and ensure accuracy. The recommended values by Taylor, et al. (2015) are used for final normalization of the samples. The methodology leads to an external precision better than 50 ppm for ^{204}Pb normalized ratios and 20 ppm for ^{206}Pb normalized ratios.

The preparation of the sample materials for chemical and lead isotopic analysis was carried out by the staff of the German Mining Museum, Bochum.

Results

Microscopic and geochemical results

Bastam Valley sites

From the four sites of Bastam Valley, eight samples (two from each site) were collected, from which only five were analyzed. All the selected samples were fragmental and measured less than 10 cm in length and width (their sizes vary between l: 4.5-8.5 cm; w: 2.2-7.3 cm; h: 1.2-2.7 cm) (Figure 8).

Sample 1 (from Cheshmeh Saleh) is a dark gray slag and shows a more or less smooth external surface with a flow texture. The thin section shows a porous but homogeneous iron/manganese silicate core. Fayalite and tephroite are two main components of the sample which are in different forms and sizes: Fine laths are more or less concentrated on the upper and lower surface, while large idiomorphic crystals are at the core. Iron oxides as very fine dendritic wüstites have grown between fayalites and are superimposed on leucite, which has a skeleton/zebra structure (Figure 9, a). They are more abundant on outer zones at the upper and lower surfaces than at the inner part of the slag. Several prills and particles of metallic iron are also scattered all across the slag and overlay the olivines (fayalites and tephroites).

Table 1a. List of analyzed slags with their dimension, mineralogical phases, and elemental characterization.

Sample no.	Lab. no.	Site	Slag type		Dimention W x L x T (cm)	Weight (gr)	XRD (main component)	XRD (secondary/ accessory component)	Mineralogic phases (microscopic observation)
1	**10120**	Cheshmeh Saleh	Smelting slag	Tap slag	4 x 4.9 x 2.4	48	Fayalite, Tephroite		Fine lathes of fayalites/tephroites near surfaces; large idiomorphic fayalites/ tephroite at the inner part; dendritic wüstites grow up superimposed on leucite with a skeleton/zebra structure between lathes of fayalites/tephroites; droplets of metallic iron scattered all over the slag.
2		Cheshmeh Saleh	Smelting slag	Tap slag	2.2 x 4.8 x 1.2	24	-	-	-
3		Kani Mar	Smelting slag	Tap slag	4.5 x 5.3 x 1.9	72	-	-	-
4	**10121**	Kani Mar	Smelting slag	Tap slag	3.5 x 5.4 x 2.7	78	Fayalite	Wüstite?, Dolomite, Ankerite / Quartz, Leucite	Lathes of fayalite near surfaces, large idiomorphic fayalites at the inner part; globular wüstites at the border of lower zone; dendritic wüstites superimposed on idiomorphic fayalites at the inner zones; cubic and octahedral magnetite at the upper surface; droplets of metallic iron scattered all over the slag.
5		Kani Qebleh	Smelting slag	Tap slag	4 x 4.5 x 2.7	60	-	-	-
6	**10122**	Kani Qebleh	Smelting slag	Bottom furnace slag	7.3 x 8.5 x 2.5	148	Fayalite, Tephroite	Leucite, Quartz, Ankerit / Hematite?	Longated lathes of fayalite/tephroite near surfaces; idiomorphic fayalites/ tephroite at the inner part; leucite as grey skeleton-zebra structure, not very rich in iron oxides: some fine dendritic and globular wüstites grow up with leucite at the upper part; some iron oxides trapped in silicious inclusions at the lower surface; cubic and octahedral magnetite; droplets of metallic iron scattered all over the slag; silicious (quartz) inclusions.
7	**10126**	Sar Merang	Smithing slag	Slag cake (SCS)	7 x 9 x 2.5	136	Cristoballite, Quartz	Calcite	Glassy-vitreous matrix goes down and forms the main core of the slag and ends in the last quarter part with a non-fully melted siliceous zone with fine grains of quartz/cristobalite and heated clay inclusions; dendritic wüstite and cubic and octahedral magnetite in different small zones; near surfaces or boundaries of some bubbles; oxidizing metallic Iron (hammerscale?); some rare iron silicate zones with fine and elongated fayalites in glassy matrix.
8	**10129**	Sar Merang	Smelting slag	Bottom furnace slag	3.7 x 5.4 x 3.6	70	Fayalite, Tephroite	Leucite, Quartz, Mellilite / Ankerit, Hedenbergite	Lathes of fayalite/tephroite; idiomorphic fayalite/tephroite + nanocrystalline olivines; globular wüstite growing up at the lower part; agglomeration of iron oxide and quartz at down-right part of the thin section; charcoal between a box work structure of iron oxides at downleft part of the thin section.
9	**10127**	Sar Merang	Smelting slag	Bottom furnace slag	5.5 x 8 x 2.5	60	Fayalite, Melilite, Tephroite	Ankerite, Dolomite, Leucite, Wüstite / Quartz	Fayalites/tephroite in different sizes and forms: lathes, idiomorphic and nanocrystalline; lathes on the upper surfaces and nanocrystalline forms at the lower surface; idiomorphic crystalline at the inner part; leucites and melilites in a skeleton/zebra structure between fayalite/tephroite and in a glassy matrix; globular wüstite superimposed on idiomorphic fayalite/tephroite, dendritic wüstite superimposed on lathes of fayalite/tephroite, octahedral and cubic magnetite at the upper surface, droplets of metallic iron scattered all over the slag, glass and silicious inclusions.

Sample no.	Lab. no.	Site	Slag type		Dimention W x L x T (cm)	Weight (gr)	XRD (main component)	XRD (secondary/ accessory component)	Mineralogic phases (microscopic observation)
10	**10128**	Sar Merang	Smithing slag	Slag cake (SCS)	5.6 x 6 x 3.8	65	Cristoballite, Quartz	Feldspar	Glassy-vitreous matrix goes down, forms the main core of the slag and ends in the last quarter part with a non-fully melted silicious zone of fine grained of quartz/cristobalite and heated clay inclusions; dendritic wüstite and cubic and octahedral magnetite in different small zones, near surfaces or boundaries of some bubbles; oxidizing metallic Iron (hammerscale?); some rare iron silicate zones with fine and elongated fayalites in glassy matrix.
11		Sar Merang	Smelting slag	?	3.8 x 5.5 x 1.1	20	-	-	-
12		Sar Merang	Smelting slag	?	4.9 x 6.5 x 3.6	80	-	-	-
13	**10125**	Sar Merang	Smelting slag	Tap slag	7 x 8 x 3.2	150	Fayalite, Tephroite	Melilite?, Leucite?, Wüstite, Dolomite, Ankerite / Quartz	Fine lathes of fayalite/tephroit near the surfaces, idiomorphic fayalites/tephroite at the inner part, free dendritic wüstites superimposed on olivines structures at the inner part, globular/filament wüstites near the lower surface, few wüstites at the upper surface, leucites and melilites grow up between fayalites with a skeleton/ zebra structure, iron oxides crusts at lower surface, grains of quartz at lower surface, droplets of metallic iron.
14	**10123**	Seyl Jengir	Smelting slag	Tap slag	4.9 x 6.1 x 1.9	116	Fayalite	Quartz, Wüstite	Lathes of fayalites near surfaces; large idiomorphic fayalites at the inner part; globular wüstites at the border of flow zone; globular wüstite intergrowing with lathes of fayalites visible in several areas; Dendritic wüstites superimposed on idiomorphic fayalites at the inner parts; cubic and octahedral magnetite at the upper surface; droplets of metallic iron scattered all over the slag and particularly at the lower part.
15	**10124**	Seyl Jengir	Ceramic	Furnace lining wall	3.2 x 5.1 x 2.4	44	Quartz, Cristobalite	Hematite	Grains of quartz and cristobalite in different sizes at the external surface, vitreous matrix at the inner surface, cubic hematite in a glassy matrix near inner surface , low amount of iron oxides.

Table 1b. List of analyzed slags with their dimension, mineralogical phases, and elemental characterization.

Sample no.	Lab. no.	ICP-MS measurments of some major & trace elements (wt.%)													
		As	Sn	Na_2O	BaO	MgO	Al_2O_3	SiO_2	SO_3	CaO	TiO_2	MnO	FeO	Cu	K_2O
1	**10120**	<0.0005	<0.0001	0.063	0.158	1.12	2.34	30.834	0.039	6.083	0.116	6.580	52.001	0.0017	0.9
2		-	-	-	-	-	-	-	-	-	-	-	-	-	-
3		-	-	-	-	-	-	-	-	-	-	-	-	-	-
4	**10121**	<0.0005	<0.0001	0.063	0.269	1.44	2.53	28.093	0.033	8.020	0.132	6.916	47.233	0.0023	1.26
5		-	-	-	-	-	-	-	-	-	-	-	-	-	-
6	**10122**	<0.0005	<0.0001	0.098	0.046	1.305	3.183	34.085	0.030	12.922	0.208	5.321	37.105	0.0018	2.31
7	**10126**	<0.0005	0.00017413	0.237	0.026	1.546	8.761	68.398	0.006	3.505	0.504	0.773	9.302	0.0064	4.55
8	**10129**	<0.0005	<0.0001	0.109	0.223	1.333	4.004	35.297	0.039	8.968	0.224	7.083	40.304	0.0047	2.045
9	**10127**	<0.0005	<0.0001	0.090	0.092	1.230	2.913	28.941	0.031	8.916	0.160	7.923	45.532	0.0017	1.71
10	**10128**	<0.0005	0.0002157	0.210	0.019	1.469	9.109	77.142	0.002	2.283	0.525	0.122	4.791	0.0074	2.39
11		-	-	-	-	-	-	-	-	-	-	-	-	-	-
12		-	-	-	-	-	-	-	-	-	-	-	-	-	-
13	**10125**	<0.0005	<0.0001	0.073	0.112	1.308	3.004	29.291	0.044	9.100	0.167	8.078	47.058	0.0018	2.02
14	**10123**	<0.0005	<0.0001	0.054	0.121	1.001	2.200	26.530	0.020	4.866	0.113	4.922	56.144	0.0091	0.68
15	**10124**	<0.0005	0.00018875	0.115	0.013	1.221	6.645	80.409	0.005	1.992	0.480	0.066	4.928	0.0048	1.65

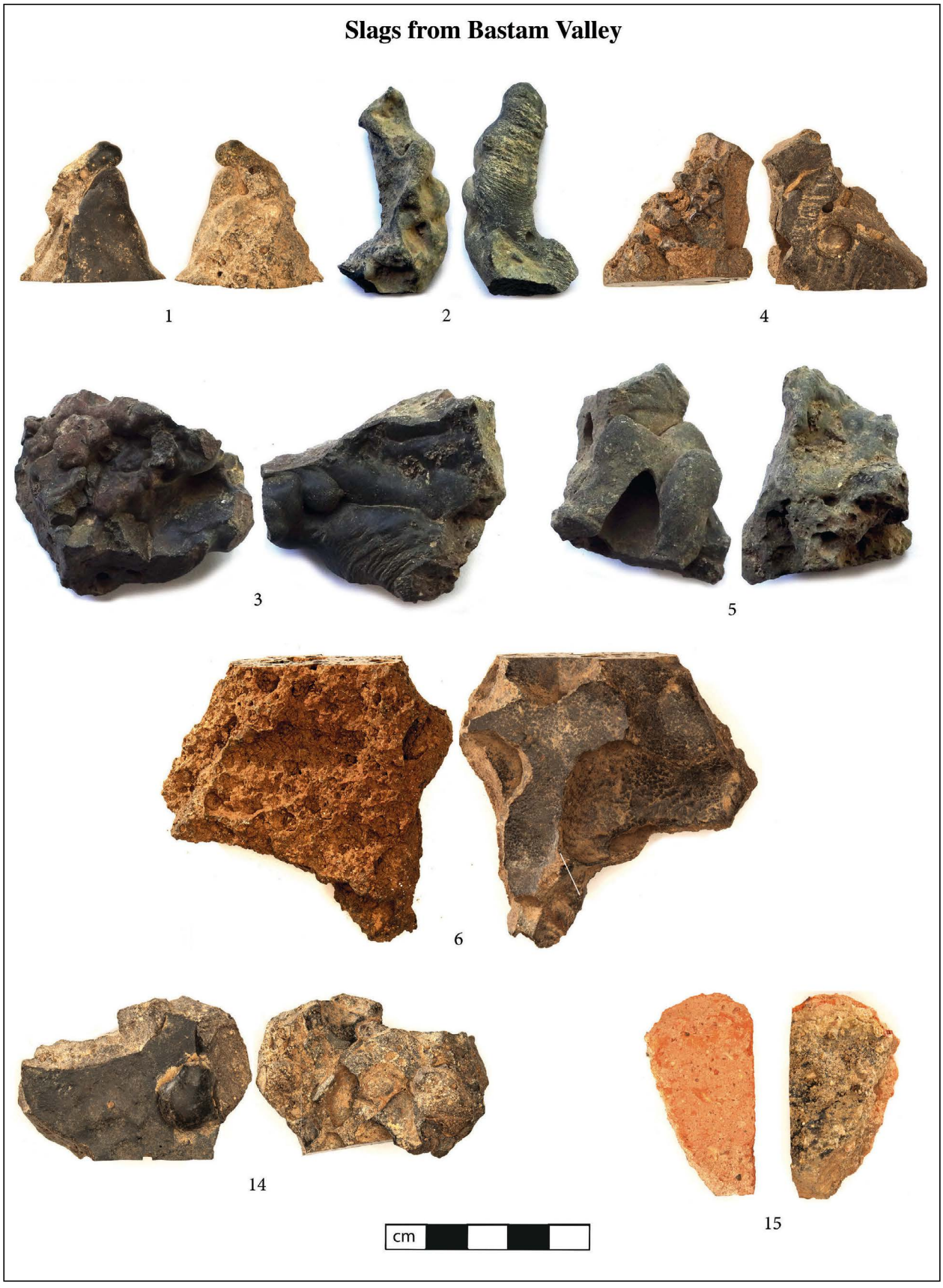

Figure 8. Photos of samples from Bastam Valley. Sample 1: slag with dark gray and smooth surface and flow texture. Sample 2: slag with a dark grey and smooth surface, flowing texture and sometimes slight waves (reminiscent of milk skin) on one side and some irregularities on the other side. Samples 3-5 and 14: slags with dark grey surfaces. Upper surfaces are smooth with flow texture. Lower surfaces show irregularities. Several flow zones overlap the surfaces. Sample 6: slag with dark grey color. Upper surface is smooth with a leather-like texture. Several elongated cavities are visible in upper surface. The lower surface is very rough. Sample 15: overheated ceramic piece with a slaggy inner side. The paste is orange with mineral inclusions. The inner slaggy side has a rough surface with a dark grey color. Photos: Z. Hashemi.

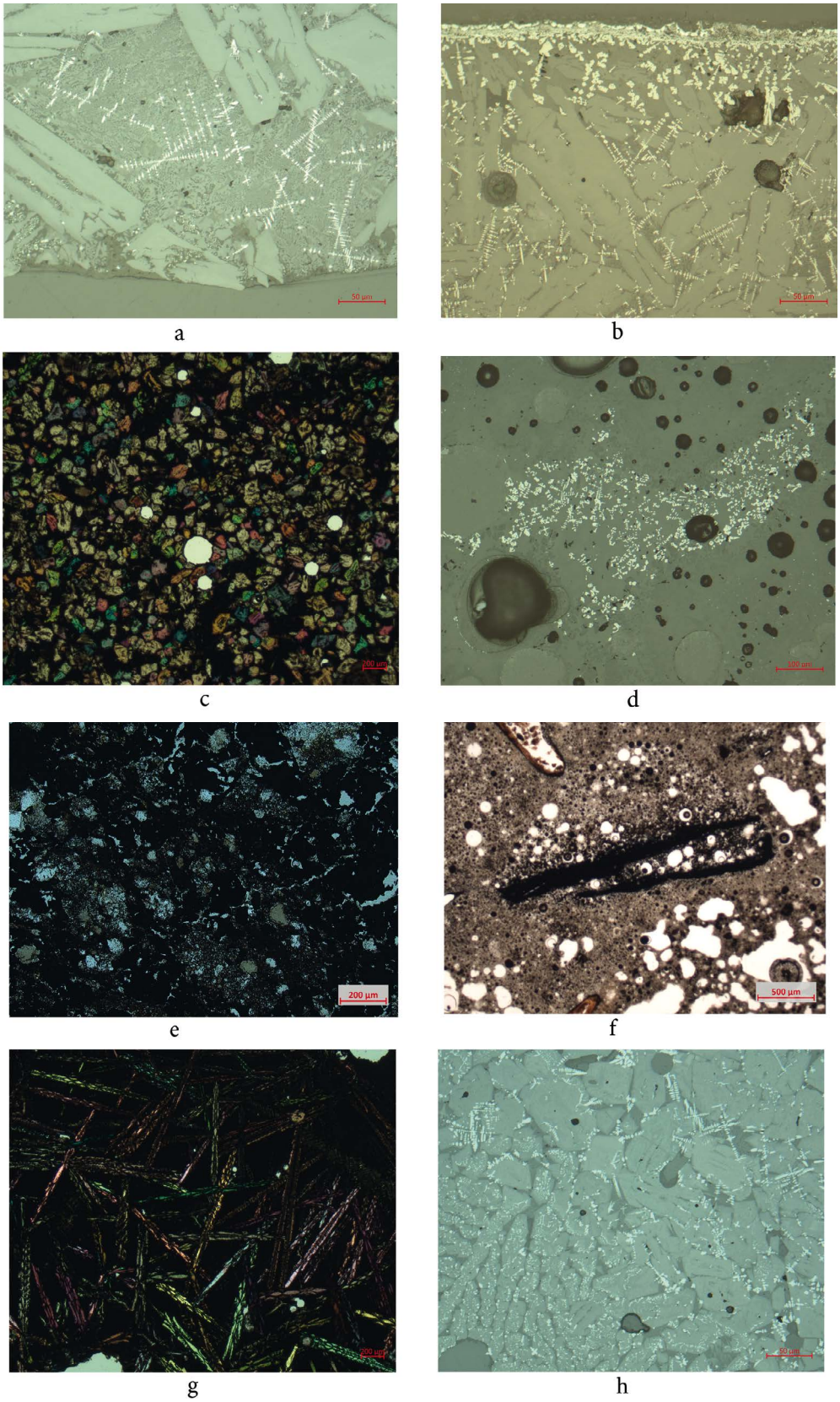

Figure 9. Microscopic photography from thin sections of some samples. a: sample 1 (Cheshmeh Saleh), dendritic wüstites superimpose on leucite with a skeleton structure and surrounded by laths of fayalites. b: sample 4 (Kani Mar), upper surface, magnetites in a cubic and octahedral structure at the edge, dendritic wüstites in the centre. c: sample 4 (Kani Mar), idiomorphic fayalites at the inner part of the slag. d: sample 7 (Sar Merang), octahedral magnetites in a glassy-vitreous matrix. e: sample 8 (Sar Merang), high concentration of iron oxides and fine grains of quartz in a glassy matrix (lower part of the slag near the side). e: sample 10 (Sar Merang), iron oxides in a vitreous-glassy matrix. It is a possible remnant of metallic iron in a very advances state of oxidizing (remnant of hammer-scale?). g: sample 13 (Sar Merang), laths of fayalites at the upper part of the slag. h: sample 14 (Seyl Jengir), dendritic wüstites at the inner part, globular wüstites at the lower surface of the slag. Scale: a, b, h = 50 µm; d = 100 µm; c, e, g = 200 µm; f = 500 µm. Photos: Z. Hashemi.

The ICP-MS analysis on the sample shows that iron oxide (FeO, 52 wt.%) and silicon dioxide (SiO_2, 30.8 wt.%) are two major components of the slag. Manganese oxide (MnO, 6.58 wt.%), calcium oxide (CaO, 6.08 wt.%), aluminum oxide (2.35 wt.%), and magnesium oxide (MgO, 1.12 %) are present in lesser amounts, as the other main components of the sample. Copper has a very low content with only 0.0018 wt.%.

Sample 2 (from Cheshmeh Saleh) is also a dark gray slag with an external smooth surface with a flow texture and slight waves (reminiscent of milk skin) on one side and some irregularity on the other side. This slag has not been analyzed. So, we cannot comment on its internal mineralogical phases nor on its trace elements, but is external characteristics leads us to put it in the same category as sample 1.

Samples 3, 4 (from Kani Mar)**, 5** (from Kani Qebleh) **and 14 (**from Seyl Jengir), have been grouped together, because of their similar porosity, their lower surface irregularity, and their richness in iron oxides in the border zones. These all demonstrate a smooth upper surface with flow texture. The lower surface of these samples shows a more or less smooth texture but with much more irregularity of forms. Several flow zones seem to overlap. Petrographic and geochemical investigations were not performed on the samples 3 and 5. But in the thin sections of samples 4 and 14, the flow structures are already visible to the naked eye. Fayalite, in different habits, is the main component of these slags. The larger crystals are even visible to the unaided eye. Fine laths of fayalites are concentrated at the border zones while idiomorphic forms occur in the inner parts (Figure 9, c). The cores of slags are less porous than their edges. Most of bubbles are concentrated on the edges. There are only few but big bubbles in the inner part of slag. These slags are rich in iron oxides in the form of dendritic and globular wüstite. Borders edges of flow zones are particularly rich in iron oxides and they are more or less in a globular or filament form. At the upper surface, the iron oxides form cubic and octahedral structures which are probably crystals of magnetite (Figure 9, b). Globules of wüstite that were grown together with laths of fayalite are visible in several areas of slag 14. Free dendritic wüstites are generally superimposed on idiomorphic fayalites of the inner parts of flow zones. Droplets of metallic iron are also visible across different areas of the slags particularly in the lower part of sample 14.

Geochemical investigation on the samples 4 & 14 demonstrates that iron oxide (FeO) with 47.2-56.1 wt.% and silicon dioxide (SiO_2) with 26.5-28.1wt.% are the two major components of the slag. Calcium oxide (CaO) with 4.87-8.02 wt.%, Manganese oxide (MnO) with 4.92-6.92 wt.%, aluminum oxide with 2.2-2.4 wt.%, and magnesium oxide with (MgO) with 1-1.44 wt.% are present in lesser amounts as other main components of the sample. Copper has again a very low content with only 0.0023-0.0091 wt.%.

Sample 6 (from Kani Qebleh) is a dark grey slag with a more or less smooth and leather-like texture at the upper surface, where several elongated cavities are visible. On the other hand, the lower surface is very rough. Crystals of fayalite together with fine crystals of tephroite are the main components of this slag. In the thin section, we can see an iron silicate core with a high porosity composed of different sizes of bubbles and also several siliceous inclusions (quartz). Fayalites, visible to the naked eye, are mostly in the form of elongated laths, but in the inner parts idiomorphic structures are also visible. At the upper surface, near the edge, laths of fayalites are mostly vertical. But the uppermost part, at the border zone is composed of a thin horizontal layer of lathes of fayalite. This slag is not very rich in iron oxides. Very fine dendritic and spherical wüstites as well as cubic and octahedral magnetite crystals have formed between the fayalites and leucites in their skeletal zebra structure. The lower surface is almost free of iron oxides. These iron oxides are only visible trapped in inclusions. Droplets and globules of metallic iron are visible scattered in different areas. A relatively large piece of metallic iron is trapped in a quartz inclusion at the middle of the slag.

The results of ICP-MS show a roughly different geochemistry compared to the other slag samples. However, iron oxide and silicon dioxide remain as main components, with their almost equal ratios: (FeO) with 37.1 wt.% and silicon dioxide (SiO_2) with 34.1 wt.%. The other main components, compared to the other samples, calcium oxide (CaO) with 12.9 wt.% has a relatively high percentage. Manganese oxide (MnO) with 5.32 wt.%, aluminum oxide with 3.18 wt.%, and magnesium oxide (MgO) with 1.32 wt.% are other main components. Copper shows a very low content with only 0.0018 wt.%.

Sample 15 (from Seyl Jengir) is a ceramic piece that has probably been exposed to very high heat, with a slaggy inside. The inner slaggy side has a rough surface with a dark grey color. Quartz and cristobalite are the main components of this sample. The petrography and trace element analyses confirm this main siliceous ingredient (80 wt.% SiO_2) has a high uniformity in the quartz and cristobalite grain size. It has a medium porosity with angular bubbles. Aluminum oxide with 6.65 wt.% is the

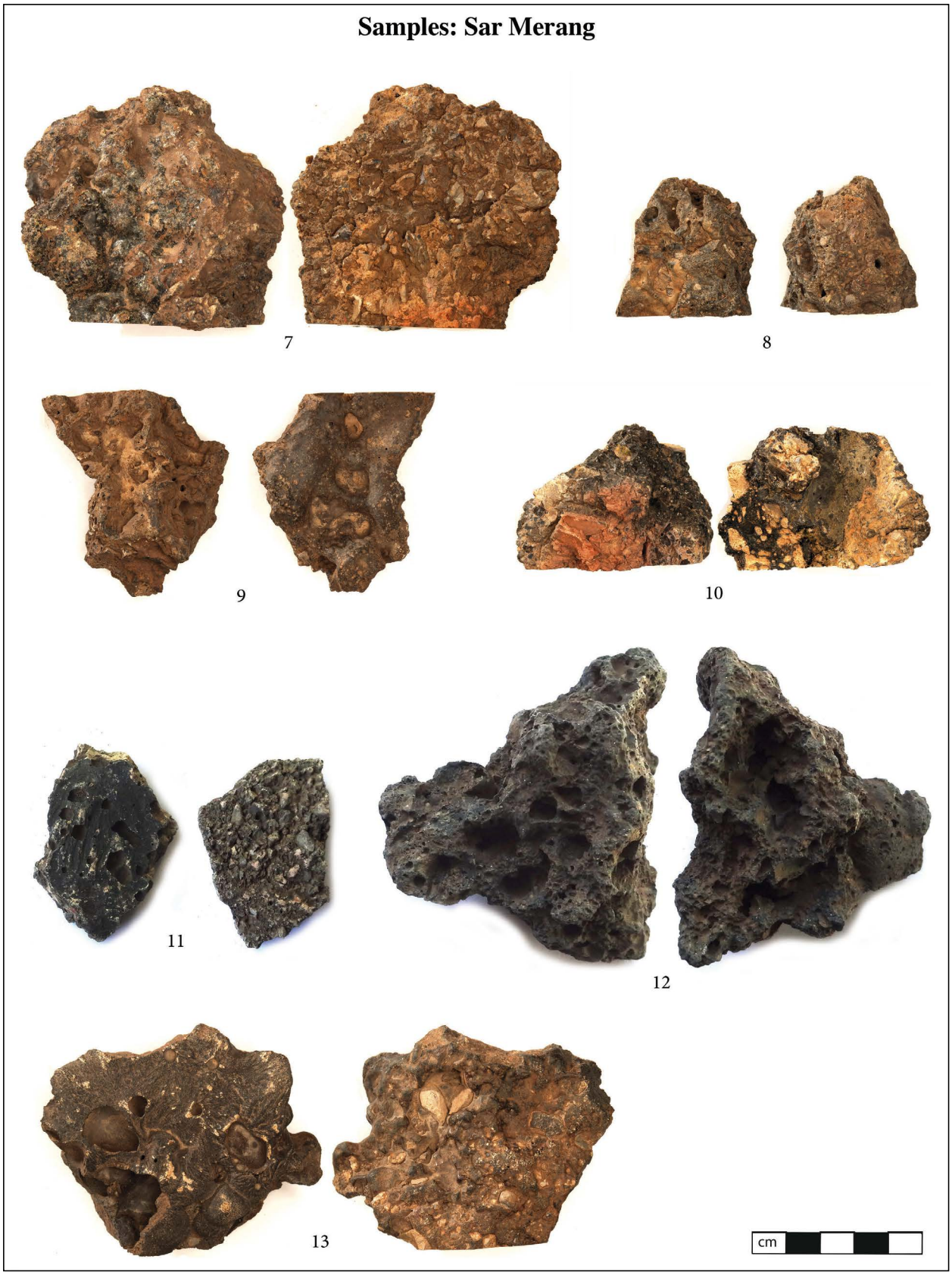

Figure 10. Photos of samples from Sar Merang. Samples 7 & 10: slags with a vitreous upper surface with many yellowish rock inclusions and a rough non molten siliceous lower surface with sandy-clayey inclusions in range of sizes. Sample 8: a slag with dark grey surface. A porous texture is visible on both the upper and lower surfaces with vacuoles and stone inclusions. Sample 9: slag with a dark grey colour and a more or less smooth but irregular upper surface. The lower surface is porous (several vacuoles) and rusty. Sample 1: fine and flat slag of a dark grey color with a more and less smooth upper surface and many pebble-sized inclusions on the lower surface. Sample 12: slag with a dark grey color. All surfaces are porous with many vacuoles. Sample 13: slag with a dark grey color. The upper surface is smooth with a flow texture. The lower surface has many inclusions in forms of gravel-pebble-sized particles. Photos: Z. Hashemi.

second main component of the sample. The inner surface has a vitreous matrix with round bubbles and low concentration of iron oxides (4.9 wt.% FeO) with cubic habit, which are probably hematite. Tis phase has been reported in XRD results as an accessory component. Calcium oxide (CaO) with 1.99 wt.%, potassium oxide (K_2O) with 1.65 wt.%, and manganese oxide (MgO) with 1.22 wt.% are lesser components. Copper has a very low content with 0.0048 wt.%.

Sar Merang

In total, seven slags are collected from Sar Merang, all fragmental and measured less than 10 cm in length and width (their sizes vary between l: 5-9 cm, w: 4-7 cm, h: 1-3.5 cm). Their weights vary between 20 to 150 grams (Figure 10).

Sample 13 demonstrates a flow texture on the upper surface and many gravel-pebble-sized particles on the lower surface. Fayalite and tephroite in different habits, sizes, and orientations are the main components. They are in the form of very fine elongated laths (Figure 9, g) on the uppermost cooling zone and visible as a flow texture from the top. Leucite and melilite, noted as secondary minerals in XRD, grow between fayalite with a skeletal structure. Iron oxide crusts and quartz grains are visible at the edge of the lower surface. Metallic iron droplets and particles are also visible within the inner part of the slag. Discrete wüstite is overlay the olivine. They have a dendritic form in the inner and upper parts and a filament or globular form at the lower surface. The upper surface is not particularly rich in iron oxides. There is a thin layer of corrosion visible on the upper surface. Bubbles are concentrated near the surface and only large bubbles within the inner part. The geochemistry of this sample shows that iron oxide (FeO) with 47.1 wt.% and silicon dioxide (SiO_2) with 29.3 wt.% are the two major components. Calcium oxide (CaO) with 9.1 wt.% and manganese oxide (MnO) with 8.08 wt.%, are other main components. Aluminum oxide (Al_2O_3) with 3 wt.%, potassium oxide (K_2O) with 2.02 wt.%, and magnesium oxide (MgO) with 1.31 wt.% contents are lesser in amount. Copper has a very low content with only 0.0019 wt.%.

Sample 9 is a dark grey slag which shows a more or less smooth but irregular upper surface with a porous (several vacuoles) and rusty lower surface. The petrography of the thin section shows a highly porous and heterogeneous core mainly formed by iron-silicates. After fayalite, melilite and tephroite are the main components of the slag. Fayalite has different habits and sizes from fine laths to idiomorphic and microcrystalline. They are very small in the lower surface and become bigger moving up to the upper surface. The border of the upper surface is covered by a small layer of fine laths of fayalite. They are also visible as lenses in different inner zones. Melilite and leucite, in a zebra skeletal structure, are present between fayalite, in a glassy matrix. Iron oxides in form of discrete wüstite are scattered all over the slag, and overlay the fayalite. They have a more globular form on the idiomorphic fayalite and a more dendritic form on elongated laths. The majority of wüstite grains are globular. The upper surface of the slag is rich in iron oxides in an octahedral and cubic habit which suggests magnetite. The round globules and droplets of oxidized metallic iron, are observed in several inner parts of the slag. The heterogeneous core of the slag contains several glass and siliceous inclusions. The geochemistry of the sample shows that iron oxide (FeO) with 45.5 wt.% and silicon dioxide (SiO_2) with 28.9 wt.% are the two major components. Calcium oxide (CaO) with 8.92 wt.% and manganese oxide (MnO) with 7.92 wt.%, are two other main components. Aluminum oxide (Al_2O_3) with 2.91 wt.%, potassium oxide (K_2O) with 1.72 wt.%, and magnesium oxide (MgO) with 1.23 wt.% content are minor. Copper has a very low content with only 0.0017 wt.%.

Sample 8 is a dark grey slag which has a porous texture on both upper and lower surfaces with vacuoles and stone inclusions. Thin section petrography shows a porous and heterogeneous core mainly formed by iron-silicate in different habits and sizes. Fayalite and tephroite are the two main components of the slag. Their crystals are visible to the bare eye. Iron oxides are rare in the main part of the slag, but their presence increase as cubic and globular grains of wüstite/magnetite at the bottom-left and bottom-right part of the slag, close to two reddish particles adhering to the slag and visible to the naked eye. Microscopic observation of these two areas shows that the right one is a mixture of fine grains of quartz, some glass and a high concentration of iron oxides (Figures 11, 4; 8, e). The left one has a box-work texture with a high concentration of iron oxides in the form of a filament inside a matrix of carbon (Figure 11, 1). Quite large tabular particles of metallic iron are also visible at the margin of this area. Metallic iron particles are visible in different areas at the core of the slag. There are also different quartz and glass inclusions. The geochemistry of the sample shows that iron oxide (FeO) with 40.3 wt.% and silicon dioxide (SiO_2) with 35.3 wt.% are two major components. Calcium oxide (CaO) with 8.97 wt.% and manganese oxide (MnO) with 7.08 wt.%, are two other main components. Aluminum oxide (Al_2O_3) is 4 wt.%, potassium oxide (K_2O) 2.05 wt.% and magnesium

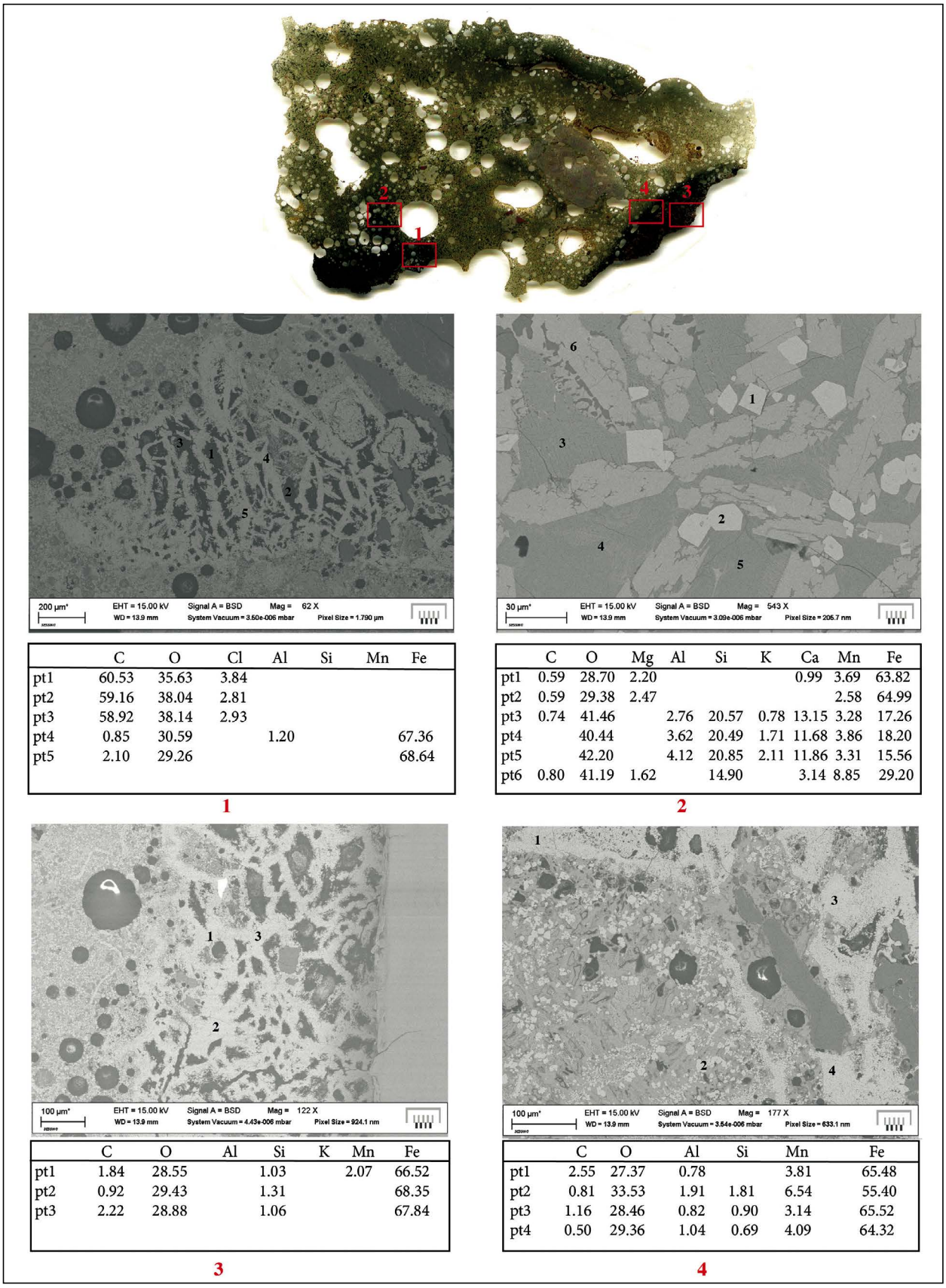

	C	O	Cl	Al	Si	Mn	Fe
pt1	60.53	35.63	3.84				
pt2	59.16	38.04	2.81				
pt3	58.92	38.14	2.93				
pt4	0.85	30.59		1.20			67.36
pt5	2.10	29.26					68.64

1

	C	O	Mg	Al	Si	K	Ca	Mn	Fe
pt1	0.59	28.70	2.20				0.99	3.69	63.82
pt2	0.59	29.38	2.47					2.58	64.99
pt3	0.74	41.46		2.76	20.57	0.78	13.15	3.28	17.26
pt4		40.44		3.62	20.49	1.71	11.68	3.86	18.20
pt5		42.20		4.12	20.85	2.11	11.86	3.31	15.56
pt6	0.80	41.19	1.62		14.90		3.14	8.85	29.20

2

	C	O	Al	Si	K	Mn	Fe
pt1	1.84	28.55		1.03		2.07	66.52
pt2	0.92	29.43		1.31			68.35
pt3	2.22	28.88		1.06			67.84

3

	C	O	Al	Si	Mn	Fe
pt1	2.55	27.37	0.78		3.81	65.48
pt2	0.81	33.53	1.91	1.81	6.54	55.40
pt3	1.16	28.46	0.82	0.90	3.14	65.52
pt4	0.50	29.36	1.04	0.69	4.09	64.32

4

Figure 11. Sample 8, slag from Sar Merang. Thin section and SEM microscopic photos. 1: reddish particles adhering to the slag, visible at the bottom left part of the thin section. The box-work texture shows a high concentration of iron oxides in form of a filament inside a matrix of carbon. It can be an adhering piece of charcoal which, over time, has been replaced by iron oxides. 2: reddish particles adhering to the slag, visible in the bottom-left part of the thin section. High concentrations of iron oxides progressively adopt a globular and cubic form (points 1 and 2) toward the core of the slag and almost disappear near the upper surface. 3 & 4: reddish particles adhering to the slag, visible in the down-right part of the thin section. It shows a mixture of fine grains of quartz, some glasses and a high concentration of iron oxides. Photos: Z. Hashemi.

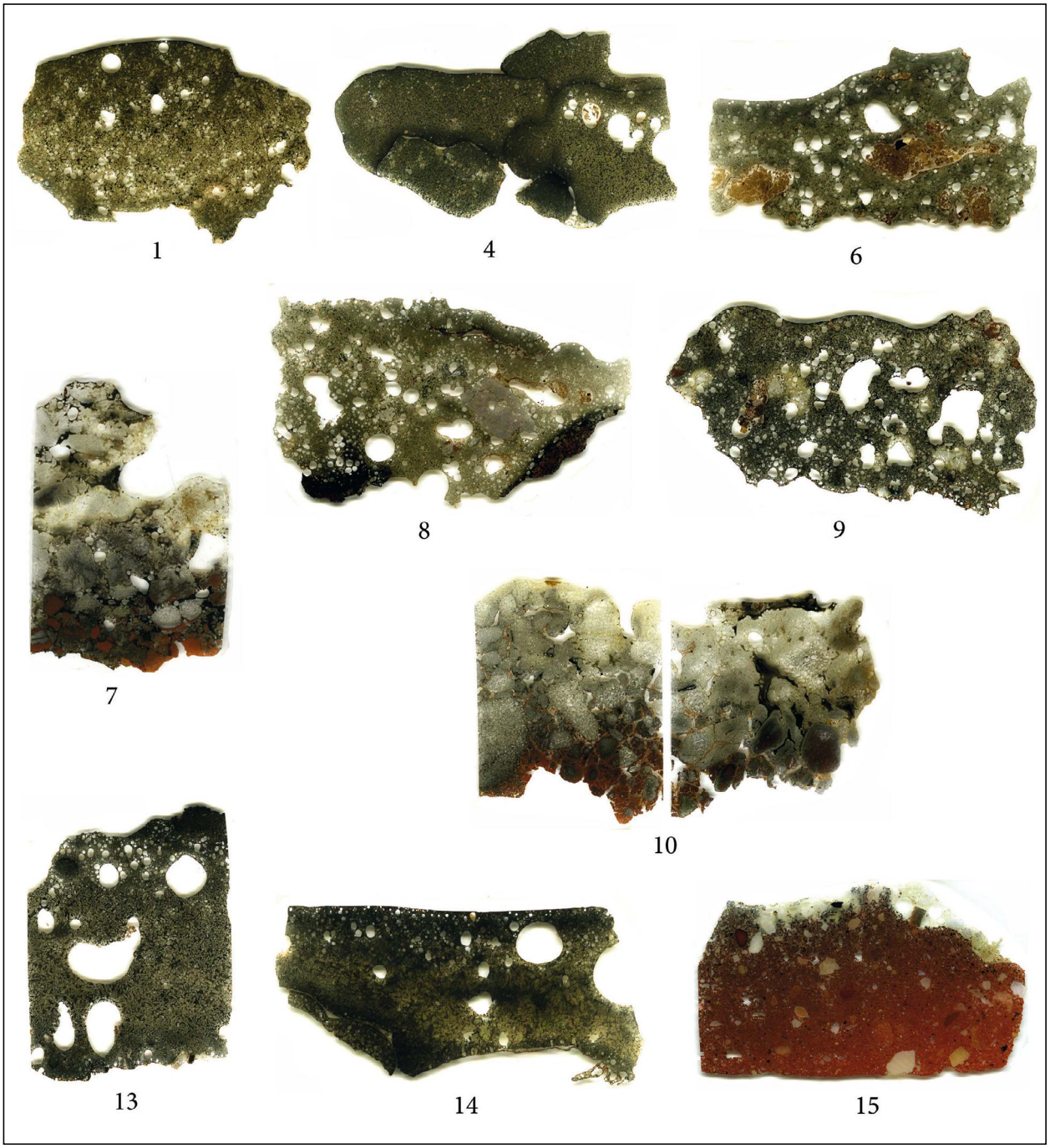

Figure 12. Thin sections of the analyzed samples: Samples 1, 4, 6, 14 & 15 are from Bastam Valley and samples 7-10 and 13 are from Sar Merang. Sample 1: thin section shows a porous but homogeneous iron/manganese silicate core. Samples 4 and 14: thin sections show overlapping flow zones inside slags. Fayalite, in different habits and sizes, is the main component of these slags. The larger crystals are even visible to the naked eye. The cores of the slags are less porous than their borders. Most of bubbles are concentrated on the borders. Sample 6: An iron silicate core with a high porosity composed of different sizes of the bubbles and also several siliceous inclusions (quartz). Sample 15: a ceramic exposed to high temperature. The paste is orange with mineral inclusions. Quartz and cristobalite are the main components of this sample. Samples 7 and 10: thin sections show a high porosity with many bubbles and heterogeneous structures. The glassy-vitreous matrix begins at the main core of slags and continues to the lower parts with a non-fully melted siliceous zone including fine grains of quartz/cristobalite and heated clay inclusions. Sample 8: a porous and heterogeneous core mainly formed by iron-silicate in different habits and sizes. Fayalite and tephroite are the two main components of the slag. Their crystals are visible to the unaided eye. Iron oxides are rare in the main part of the slag, but their presence increases abruptly at the bottom-left and bottom-right part of the slag, close to two reddish particles adhering to the slag and visible to the bare eye. Microscopic observations of these two areas show that the right one is a mixture of fine grains of quartz, some glass and a high concentration of iron oxides. The left one shows a box-work texture with a high concentration of iron oxides in form of a filament inside a matrix of carbon. Sample 9: a highly porous and heterogeneous core mainly formed by iron-silicates. The heterogeneous core of the slag contains also several glass and siliceous inclusions. Sample 13: an iron silicate core with some porosity. Bubbles are concentrated near the surface and only big bubbles in the inner part. Some iron oxide crusts and some quartz grains are visible at the border of the lower surface. Photos: Z. Hashemi.

oxide (MgO) 1.33 wt.%. Copper has a low content with only 0.0047 wt.%.

Samples 7 and 10 show a vitreous upper surface with many yellowish rock inclusions and a rough unmelted siliceous lower surface with sandy-clayey inclusions with a variety of sizes. Thin sections of both slags show a high porosity with many bubbles and a heterogeneous structure. The glassy-vitreous matrix starts at the main core of the slags and continues to the lower parts with a non-fully melted siliceous zone including fine grains of quartz/cristobalite and heated clay inclusions. Cristobalite and quartz are the main components. Rare iron silicate zones with fine and elongated fayalite are visible in some parts of the glassy-vitreous zone as well as between these and non-melted siliceous zones. They contain dendritic wüstite. Dendritic wüstite, as well as cubic and octahedral magnetite, are visible in parts of the glassy matrix, near upper surfaces or boundaries around some bubbles (Figure 9, d). Oxidized metallic iron particles are also visible in both zones. In some cases, they seem to be forming rectangular shape (Figure 9, f). The geochemistry of the samples shows that silicon dioxide (SiO_2) with 68.4-77.1 wt.% is the major component of the two slags. It is followed by aluminum oxide (Al_2O_3) with 8.76-9.11 wt.% and iron oxide (FeO) with 4.7-9 wt.%. Potassium oxide (K_2O) with 2.33 - 4.55 wt.%, calcium oxide (CaO) with 2.28-3.51 wt.%, and magnesium oxide (MgO) with 1.47-1.55 wt.% come after. By contrast to the other samplesmanganese oxide (MnO) content is much less (0.77-0.12 wt.%). Copper, as in all other samples, has a low content of 0.0064-0.0075 wt.%.

Sample 11 is a fine and flat fragmental slag of dark grey color, with a slaggy upper surface and many pebble-sized inclusions at the lower surface. **Sample 12** is a dark brown slag, porous on its all surfaces with many vacuoles. These two last slags have not been analyzed.

Patterns of Rare Earth Elements (REEs)

In order to determine whether the geochemical pattern of Rare Earth Elements (REEs) in the slag samples would show a meaningful differentiation, they were plotted on a chondrite normalized diagram based on McDonough and Sun (1995) (Figure 13). Rare Earth Elements are composed of the lanthanide series of chemical elements together with yttrium and scandium, which are split into two groups, light rare earths (LREE, including La, Ce, Pr, Nd, Sm, and Eu) and heavy rare earths (HREE, including Gd, Tb, Dy, Ho, Er, Tm, Yb, Lu, and Y) (Zhan, et al., 2023). These elements show lithophilic characteristics (Goldschmidt, 1937; Connelly, et al., 2005), therefore, one can expect that in the course of metallurgical processes, these elements would rather migrate from the ore into the silicate phase of the slag rather than into the final metal object.

All the investigated samples show a relatively similar pattern in their REE distribution. Nevertheless, a more detailed examination of the samples' REE-patterns indicates that some samples demonstrate closer REE patterns than others. In this regard, we can categorize the samples based on the similarity of their REE patterns into three different groups: group 1 including samples 1 and 14 showing almost identical LREE values except for Eu, while rather similar contents of HREE, especially in case of Er and Ho; group 2 comprising of samples 7 and 10 with very similar values for all REEs although not exactly for Tb, Gd, and Ho; and group 3 including samples 4, 6, 8, 9, 13, and 15 in which the HREE contents are more or less close but the LREE values differ in individual cases. Anyhow, samples 8 and 15 indicate slightly different patterns from the rest of the group 3 and, therefore, can also be considered as a unique sample. Very interestingly, this REE-based geochemical categorization matches well with the results of lead isotope studies (which is discussed in the following section).

In addition, the REE patterns of six Fe-Mn ore samples from the mine of ShamsAbad (average contents measured by LA-ICP-MS, Ehya and Marbouti, 2021), one ore sample from BabaAli mine (Measured by ICP-MS, Zamanian and Radmard, 2016), and several unaltered slag inclusions from five ancient Luristan ferrous artifacts (average contents measured by LA-ICP-MS, Stepanov, et al., 2020) were also compared with the studied slag pieces in order to examine for any the possible matches. Metallurgical processes could alter the original REE pattern of the ore, nevertheless, due to the lithophilic nature of REEs, it is expected that the REE concentration of the ores should be rather homogeneously transferred into the slag rather than in the final metallic iron product. Comparison between the REE patterns of the ShamsAbad ore and of the slags indicates an obvious increase in the Eu content, while a sharp decrease in the Ce content (Figure 13, a). If the ores of ShamsAbad were used for production of the studied slags, we should have normally not seen a decrease in the Ce content, because this element would not usually concentrate in the final iron phase (since it is also lithophilic), and therefore the content should not have gone down. It seems that the ShamsAbad ore did not play a role in the production of the studied slag. The REE pattern of the BabaAli iron ore (Zamanian and Radmard, 2016) reveals much lower

Table 2. ICP-MS analysis results for the REE concentrations in the slag samples (in ppm).

Sample no.	Site	REE values of the studied samples measured by ICP-MS (in ppm)													
		La	Ce	Pr	Nd	Sm	Eu	Tb	Gd	Dy	Ho	Er	Tm	Yb	Lu
1	Cheshmeh Mahi	7.2459	15.3123	1.7187	7.3991	2.0007	1.0445	0.4328	3.2193	2.3245	0.3437	0.9925	0.0922	0.8935	<0.1
4	Kani Mar	8.5414	17.8155	1.937	8.3245	2.0192	0.716	0.3585	2.8721	2.229	0.3779	1.3711	0.1321	0.9383	<0.1
6	Kani Qebleh	9.4931	19.2898	2.3061	9.7447	2.8141	0.8673	0.4425	3.5118	2.5062	0.404	1.2871	0.1229	0.9687	<0.1
7	Sar Merang	22.781	52.011	5.1159	20.7119	4.4067	0.8776	0.5915	3.495	3.5947	0.6778	2.0454	0.2333	1.8088	0.1721
8	Sar Merang	13.1781	28.86	3.1644	12.4719	3.8812	1.3537	0.6323	4.4484	3.3428	0.5398	1.5352	0.1901	1.1291	0.1461
9	Sar Merang	8.7204	20.2117	2.0794	8.8511	2.8584	1.1804	0.5701	3.7472	2.998	0.4463	1.2153	0.1393	1.1281	0.1096
10	Sar Merang	22.793	51.0751	5.1471	19.9155	4.4043	0.955	0.4765	3.9887	3.4714	0.5781	1.8635	0.2332	1.6621	0.1786
13	Sar Merang	9.5929	19.8882	2.3792	9.2066	2.8981	1.3311	0.6099	4.7923	3.5053	0.5254	1.3387	0.1464	1.0218	<0.1
14	Seyl Jengir	6.9375	15.4539	1.7204	7.3371	2.0467	0.8002	0.3279	2.1983	1.8399	0.3211	1.0215	0.0681	0.7394	<0.1
15	Seyl Jengir	19.7775	38.7212	4.4578	16.5404	3.4863	0.7978	0.42	3.2244	2.5321	0.5231	1.7302	0.1667	1.2964	0.1609

Table 3. Lead isotope analyses results for the slag samples.

		LIA Results of studied samples									
Sample no.	Site	$^{206}Pb/^{204}Pb$	2SE	$^{207}Pb/^{204}Pb$	2SE	$^{208}Pb/^{204}Pb$	2SE	$^{207}Pb/^{206}Pb$	2SE	$^{208}Pb/^{206}Pb$	2SE
1	Cheshmeh Mahi	18.4706	0.0005	15.6617	0.0004	38.6310	0.0011	0.847931	0.000008	2.09150	0.00002
4	Kani Mar	18.5791	0.0005	15.6641	0.0005	38.7049	0.0012	0.843110	0.000010	2.08324	0.00003
6	Kani Qebleh	18.6203	0.0005	15.6677	0.0005	38.7377	0.0013	0.841434	0.000007	2.08040	0.00002
7	Sar Merang	18.7318	0.0005	15.6757	0.0004	38.9490	0.0011	0.836857	0.000007	2.07932	0.00002
8	Sar Merang	18.5818	0.0004	15.6684	0.0004	38.7272	0.0011	0.843217	0.000008	2.08415	0.00003
9	Sar Merang	18.6517	0.0005	15.6781	0.0004	38.7883	0.0011	0.840573	0.000009	2.07962	0.00003
10	Sar Merang	18.7274	0.0005	15.6771	0.0005	38.9233	0.0011	0.837124	0.000008	2.07840	0.00003
13	Sar Merang	18.6017	0.0006	15.6758	0.0006	38.7130	0.0013	0.842708	0.000010	2.08114	0.00003
14	Seyl Jengir	18.4415	0.0005	15.6571	0.0005	38.6138	0.0014	0.849013	0.000006	2.09385	0.00003
15	Seyl Jengir	18.5764	0.0005	15.6676	0.0005	38.7595	0.0014	0.843418	0.000009	2.08651	0.00004

contents for most of the Rare Earth Elements, while the slag inclusions in the Luristan iron artifacts (Stepanov, et al., 2020) demonstrate much higher values for all elements (Figure 13, b). Therefore, it can be interpreted that also these ore and objects were not related to the studied slag pieces.

Lead isotope analyses

Although the lead isotopic investigations have not been commonly used for the study of iron ore, due to the reasonable (and measurable) lead content in the slag samples together with the fact that some of the iron deposits to the east and north of the study area contain lead (e.g. Ahangaran deposit), the attempt was made to gain more information about the relevance of the findings by means of lead isotope analysis. On the other hand, Schwab, et al. 2006 have already suggested lead isotope investigations as a tool for the provenance of iron artifacts. Degryse, et al. (2007) have suggested strontium isotope ratios for the provenance of iron artifacts and ore, nevertheless, since such signatures for the Iranian ore deposits have rarely been reported, we dispensed with the costs and efforts in this regard. Iron isotope measurements, as Milot, et al. (2016) have suggested for ancient iron metals tracing were not available to the authors for investigation.

The analyzed samples indicate a lead content between 4.1 to 29 ppm; the lead content of the smelting slags shows between 4.1 to 29 ppm lead (average 10 ppm), while the smithing slags indicate 13 to16 ppm lead (average 14 ppm).

The measured isotopic ratios of $^{207}Pb/^{206}Pb$ and $^{204}Pb/^{206}Pb$ and $^{208}Pb/^{204}Pb$ and $^{206}Pb/^{204}Pb$ (Figures 14 and 15) for ten slag samples indicate that the samples plot in a relatively small range. For example, all samples are between 0.837 and 0.849 for $^{207}Pb/^{206}Pb$ and 0.0534 and 0.0542 for $^{204}Pb/^{206}Pb$. Nevertheless, 3 similar

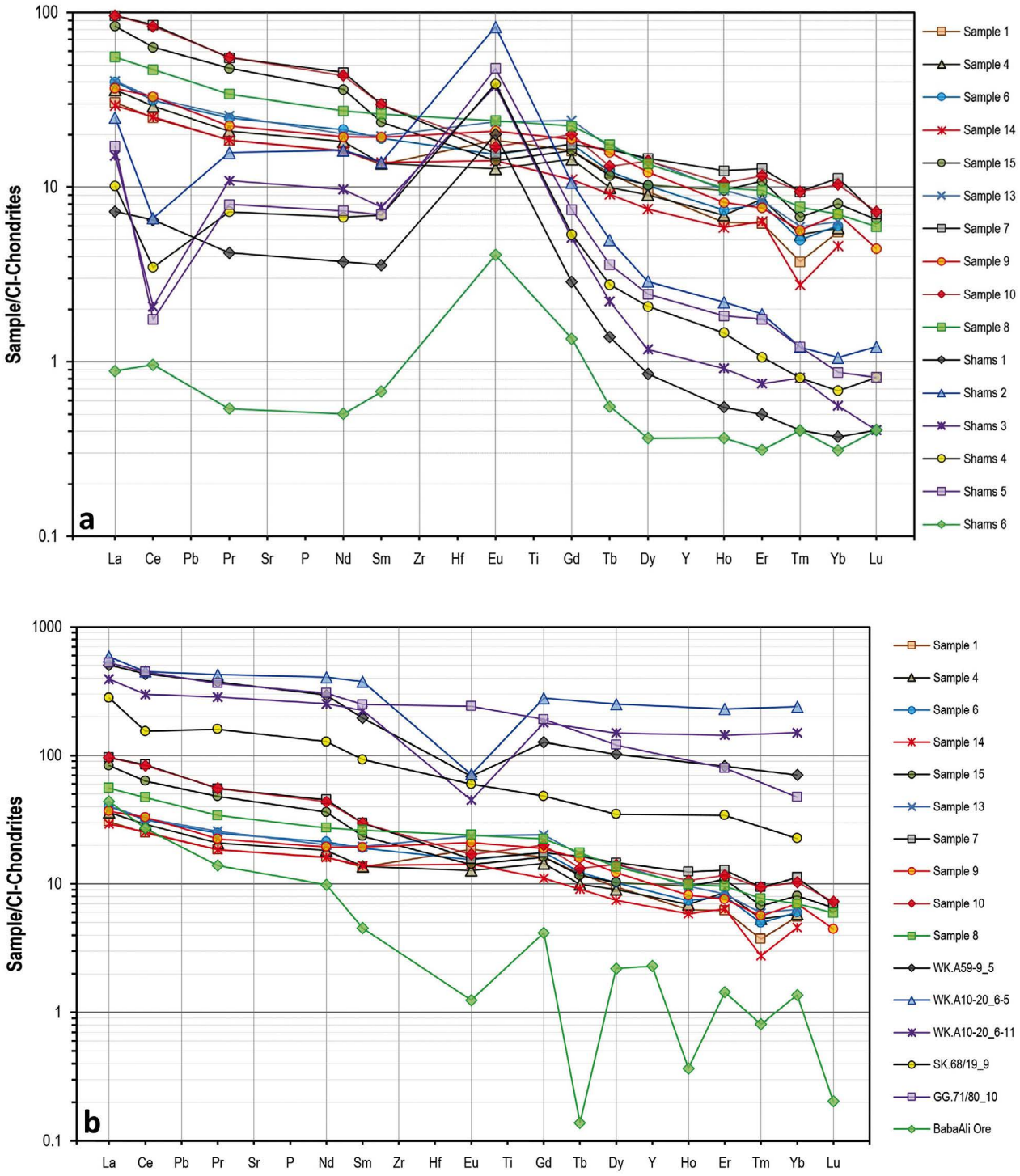

Figure 13. Chondrite-normalized (McDonough and Sun, 1995) REE patterns for the slag samples of this study compared to the same patterns of (a) the ShamsAbad ore samples (Ehya and Marbouti, 2021), and (b) the BabaAli ore sample (Zamanian and Radmard, 2016) as well as slag inclusions in five Luristan bronze artifacts (sample numbers initiated with WK, SK, and GG, Stepanov, et al., 2020).

groups can be identified from both diagrams. Group 1 contains two slags, one from Ceshmeh Saleh (sample 1) and one from Seyl Jengir (sample 14). Group 2 is composed of slags from Sar Merang (sample 7 & 10), and the third group contains the remaining slags from Kani Mar (sample 4), Kani Qebleh (sample 6) and Sar Merang (sample 8, 9 & 13) as well as one from Seyl Jengir (sample 15). It is of interest that, this categorization based on the lead isotope signatures matches well with the assortment of the same samples based on REE geochemical patterns.

The isotopic results of the slag samples were then compared to the lead isotope ratios of some mines in the region whose Pb-ratios were available including the

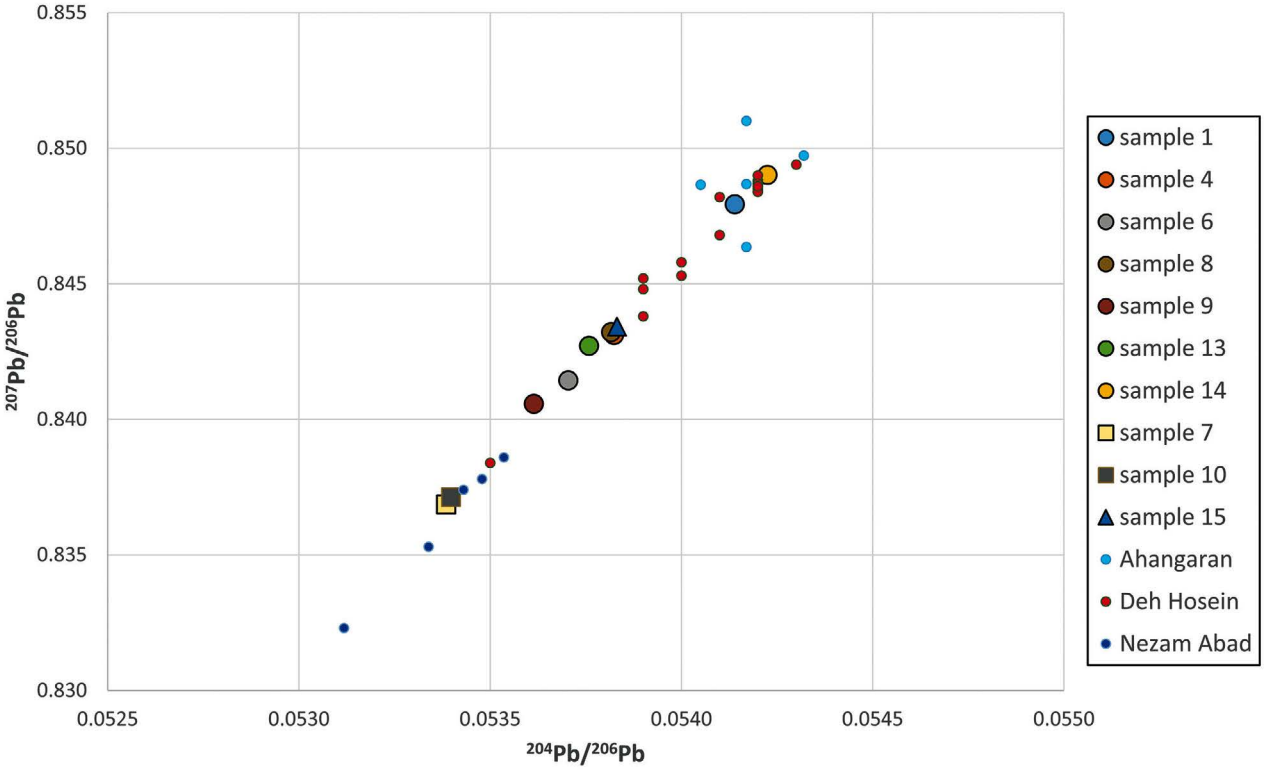

Figure 14. $^{207}Pb/^{206}Pb$ vs. $^{204}Pb/^{206}Pb$ ratios of the slag finds and furnace lining, sorted by find type. Circle = smelting slags, square = smithing slags, triangle = furnace lining.

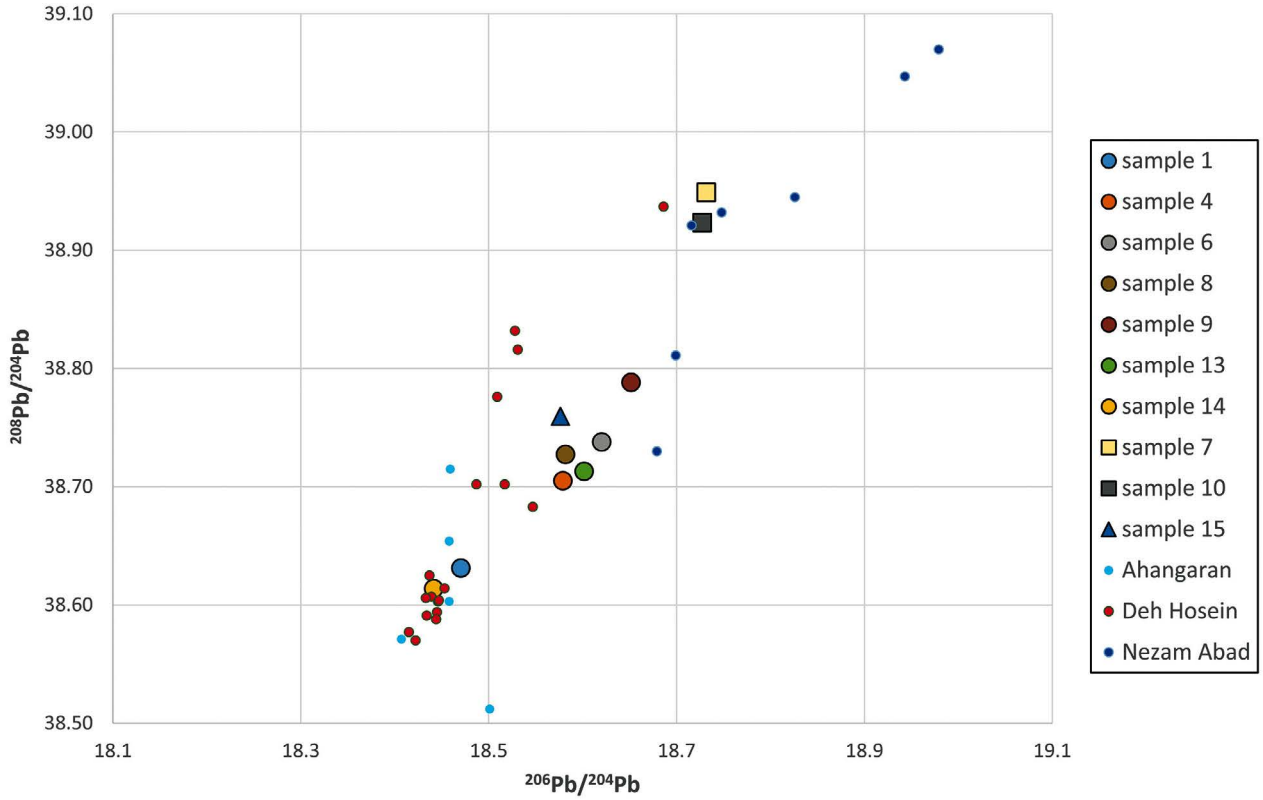

Figure 15. $^{208}Pb/^{204}Pb$ vs. $^{206}Pb/^{204}Pb$ ratios of the slag finds and furnace lining, sorted by find type. Circle = smelting slags, square = smithing slags, triangle = furnace lining.

Ahangaran Pb-Zn-Fe-Ag mine (Momenzadeh, et al., 1979; Maanijou, et al., 2020), the Deh Hosein Cu-Sn-As-Pb-Bi-W-Fe mine (Nezafati, 2006; Nezafati, Pernicka and Momenzadeh, 2009), and the Nezam Abad W-Cu-Sn mine (Nezafati, 2006; Nezafati, Pernicka and Momenzadeh, 2009) which all show traces of ancient or old workings. The lead isotope results of all three mines indicate that there is a fluctuation in the lead isotope ratios of the ore (Nezafati, 2006; Maanijou, et al., 2020). Nevertheless, the lead isotope ratios of the Ahangaran mine plot rather closely to the group 1 of the slag samples (samples 1 & 14). The lead isotope signatures of group 2 (samples 7 & 10) demonstrate a good match with part of the ore from Deh Hosein and Nezam Abad, while group 3 (samples 4, 6, 8, 9, 13 & 15) shows more or less similar ratios with the ore of Deh Hosein and Nezam Abad.

Even if the origin of the source material cannot be identified in this way, it can be assumed that the raw materials of each individual group come from deposits with similar lead isotope signatures, and this in the case of group one could be from the Ahangaran mine, while in the case of groups 2 and 3, Deh Hosein and Nezam Abad can be considered as source candidates although they do not match very well from the trace elemental patterns point of view. In fact, since Deh Hosein and Nezam Abad are mainly enriched in copper, tin, arsenic, gold and base metals rather than iron, the contribution of their ore to the production of the studied slags cannot be confirmed.

Anyhow, it seems that the mineral deposits of the central and northern part of the Sanandaj-Sirjan metallogenic zone of Iran (Nezafati, 2006; Nezafati, Pernicka and Momenzadeh, 2009) have probably provided the ore for production of the slags.

Discussion

Iron silicates (fayalite, tephroite), iron oxides (wüstite, magnetite), and glass are the main components of the samples of this study. Such mineralogical phases are the main constituents in both copper and iron slags. Therefore, they can be easily confused with each other (Hauptmann, 2020, p.368) and we cannot securely determine if samples of this study are of copper or iron working process. However, generally, for ancient copper slags we should have at least very small amounts of copper. It is striking that all samples have a very low copper content with a distribution of 0.0017 to 0.0091 wt.% (Table 1). This tilts the balance towards iron production. The other less likely possibility is that we may be facing a very efficient technology of copper production where all copper is already separated from the gangue.

Samples 1, 4, 6, 8, 9, 13 & 14 can broadly be of iron bloomery rather than a blast furnace because of their high concentration of FeO (Pleiner, 2000, p.255; Hauptmann, 2020, p.366, Fig.5.31). These heavy, dark grey or black samples have an iron oxide content (FeO) greater than 37 wt.% while silicon dioxide values (SiO_2) are less than 36 wt.%. These samples can be divided into three subgroups based on their main iron and silicon contents (Figure 16):

Iron silicates combined with quantities of iron oxides can be the main components of the smelting as well as the smithing process. One of the indicators which help to differentiate smithing from smelting slag is the amount of manganese (Pleiner, 2006, p.116, 119). Although the amount of manganese depends on the original ore, most of this lithophile component is generally transferred to the slag as tephroite (Mn_2SiO_4) during the smelting process. So, only a very low amount of manganese stays with the forged bloom following smithing. Up to 4-5 wt.% of MnO is considered a high value and indicates a smelting process rather than smithing (Pleiner, 2006, p.116, 119). The amount of MnO in the samples of 1, 4, 6, 8, 9, 13 & 14 is between 4.9 and 8 % which is quite high (Table 1). Therefore, these slags could be broadly be associated with iron smelting rather than iron smithing,

Samples 1-5, 13 & 14, with a high density and dark gray smooth surfaces, marked by flow textures can be probably classified as smelting tap slag, showing that the slag flowed out of the furnace in a liquid state (Serneels, 1993, Fig.38). Lower irregular surfaces of these samples are marked by different surfaces on which the slag is tapped such as previous cooled tap slags or pebbles at floor (on the site's surface). Thin sections of samples 4 & 14, show different flow zones. Generally, tap slags have a high homogeneity and a relatively dense core with a few large bubbles or small bubbles near the surface (Pleiner, 2000, p.262). This is what we can see especially in the samples 4, 13 & 14. In addition, as tap slag flows out of the furnace while hot and fluid, there will be a rapid cooling, during which fayalite crystalizes in an elongated, skeletal, and tubular structure (Serneels, 1993, p.25; Hauptmann, 2020, p.258). Microscopic observation of samples 1, 4, 13 and 14 show fine laths of fayalite at the border zones, in contact with outside atmosphere (Figure 9, g). These slags are also rich in wüstite (FeO) which is the result of an oversaturation of iron in the system, ejected as iron oxides while the fayalitic slag mass cools (Serneels, 1993, pp.22-24). Wüstite generally forms when the temperature is above 570°C, while below this temperature; magnetite (Fe_3O_4) is produced (Serneels, 1993, p.22). Thus, the high concentrations of wüstite in-

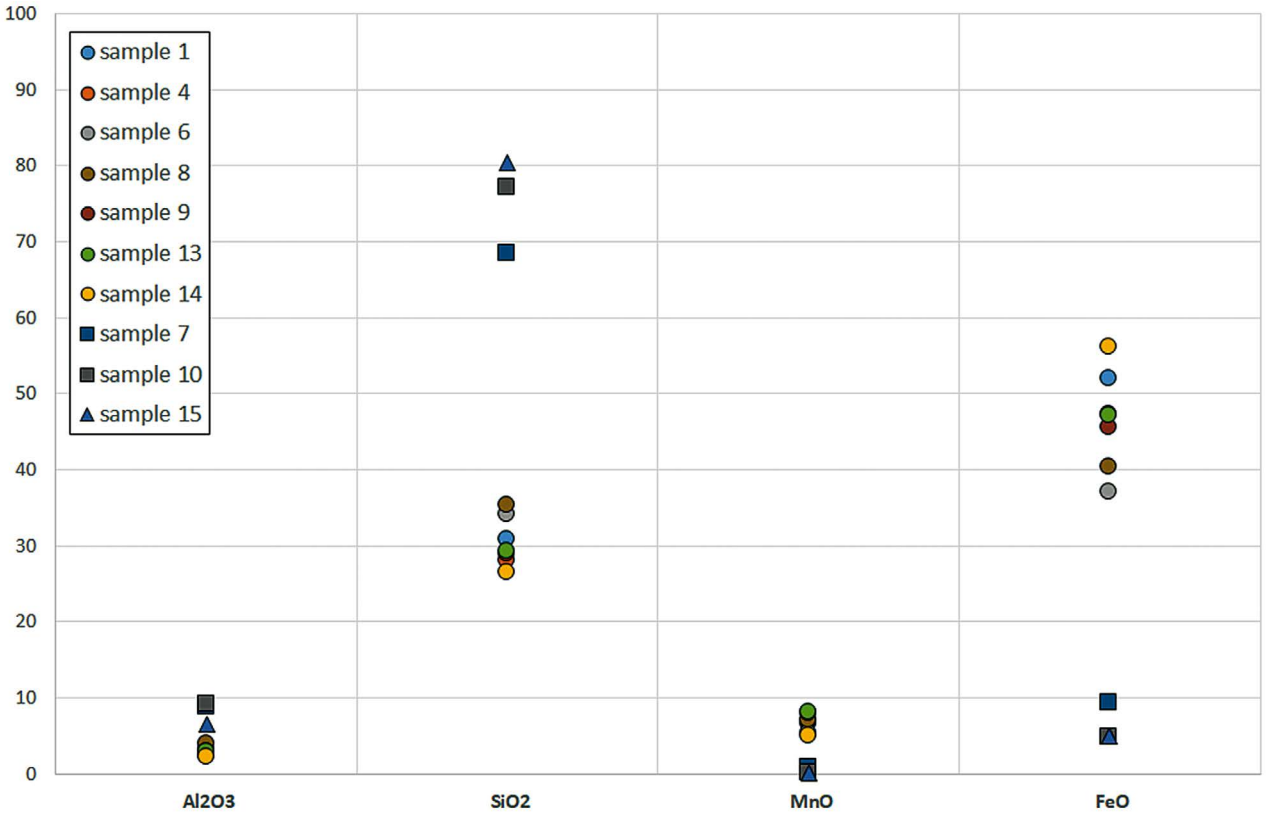

Figure 16. Diagram of the most important slag-forming elements (wt.%), measured using SC-ICP-MS, find type. Circle = smelting slags, square = smithing slags, triangle = furnace lining.

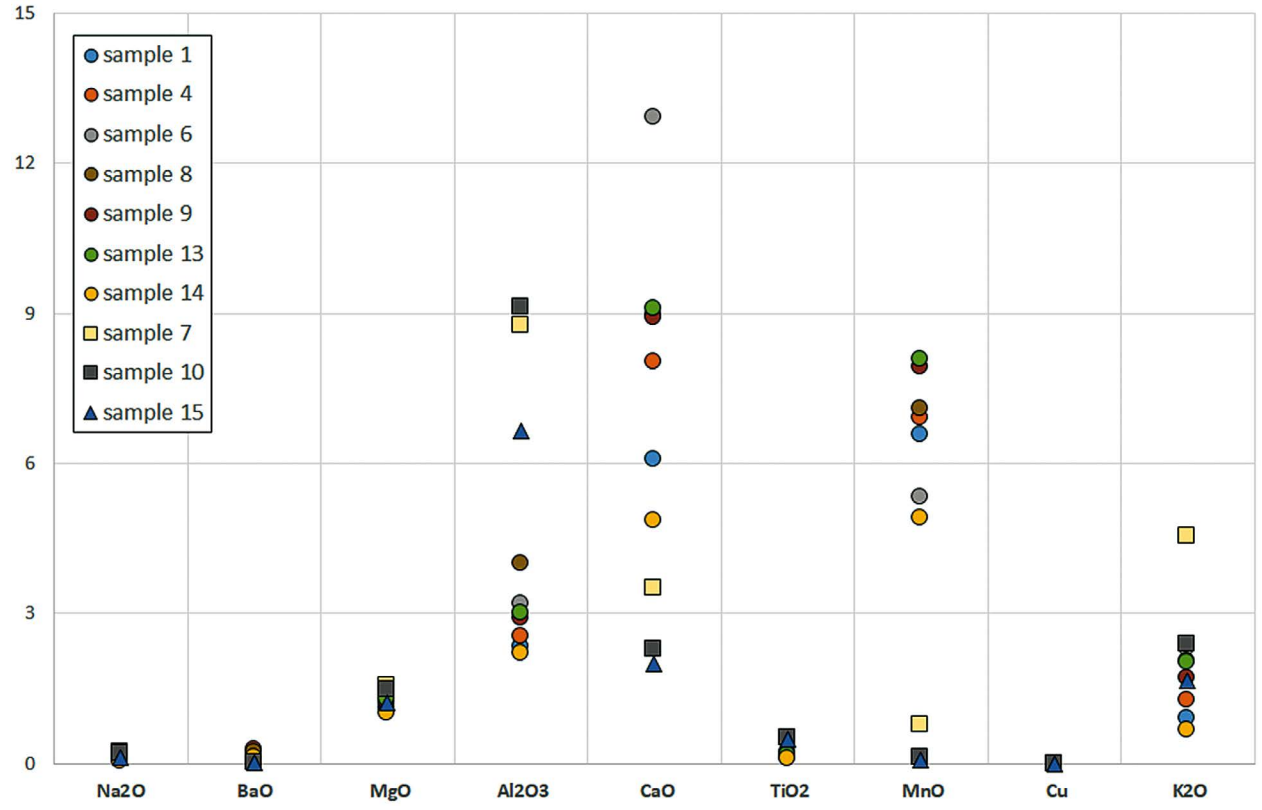

Figure 17. Diagram of the main elements (wt.%) of all finds including copper (without iron and quartz), measured using SC-ICP-MS, find type. Circle = smelting slags, square = smithing slags, triangle = furnace lining.

dicate a hot oxidation. If the formation takes place in the liquid state, wüstite crystallizes in a globular or dendritic structure. In tap slags, wüstite generally has a dendritic form but at outside edges of the flow structures it is more or less globular (Figure 9, h). At the limit of the upper surface, in contact with the outside atmosphere, when the liquid slag is exposed to high oxidizing conditions, it is magnetite which forms as a cubic and octahedral structure (Figure 9, b). All these phenomena (dendritic wüstite at the core, globular wüstite at the touchpoints of flow zones and cubic/octahedral crystals of magnetite at the upper surface) are visible in samples 4, 13 & 14, which confirm that they are tap slags.

Sample 6, both in its external and internal appearance differs from abovementioned slags. It has smooth leather like texture on the upper surface. Some elongated cavities on the surface could have been caused by air being blown in. They would indicate proximity to the tuyère. The rough lower surface confirms contact with the soil. Inside the slag, thin section analysis shows a homogeneity, a high porosity, and low amount of iron oxides. These can be considered as indications of furnace slag, where contact with charge of the furnace makes a heterogeneous and porous texture. In a slow cooling process, crystals of fayalite have time to grow up and often crystallize in idiomorphic forms (Hauptmann, 2020, p.258), however, the iron oxides content of this sample is less than the same content in the tap slags. Particles of metallic iron, due to their high density, move downwards to the bottom of the furnace and adhere to the lower surface of the slag as nodules, globules, or filaments. This phenomenon, visible in the sample 6 is also a bottom furnace slag indication. Unmelted siliceous inclusions (such as quartz) are probably the remains of detached pieces of furnace wall, fallen inside, or otherwise possibly part of the flux added to lower the melting point.

In the sample 8, several characteristics such as the absence of a flow texture, the porosity and heterogeneity of the core as well as the rarity of iron oxides in the upper surface are the indications, which lead us to suppose it is a furnace bottom smelting slag. A very interesting phenomenon can be observed in two areas at the lower part of this slag: In both right and left sides, there is a very high density of iron oxides. The macro-observation of the right one confirms a reddish adhered material. The microscopic observations and SEM analyses identified this as a combination of iron oxides, as hematite (68 wt.% of iron, 29 wt.% of oxygen) together with fine grains of quartz in a glassy matrix (Figures 3, 4, 11; 9, e). This adhered material can be part of the ore which did not have enough time to melt through the smelting process or it can be part of the emerging bloom adhering to the slag. The microscopic observations and SEM analyses of the second material at the left lower side of the slag showed also a high concentration of iron oxides, probably hematite (68 wt.% iron, 30 wt.% oxygen), in a boxwork texture with a high amount of carbon (60 wt.%. Interpretation of this phenomenon is more complicated. It can be an adhering piece of charcoal which, over time, was replaced by iron oxides (Figure 11, 1). These high concentrations of iron oxides in these two lower sides of the slag progressively take a globular and cubic form toward the core of the slag (Figure 11, 2) and almost disappear near the upper surface.

In the sample 9, the upper surface is smooth but with no evidence of a flow texture. The thin section confirms a porous core. Idiomorphic fayalites are the main component. There is a high quantity of globular wüstite with a little dendritic wüstite. It seems that this sample is a bottom furnace smelting slag. Quartz and other silicate inclusions are probably part of the detached lining wall of the furnace.

As mentioned above, three samples of 7, 10 & 15 seem not to be smelting slags. Among them, sample 15, by its ceramic part on one side and a vitreous surface on the other side is most probably part of a furnace lining wall. The slaggy surface is the inner part of the furnace, where the wall was in contact with the furnace charge Its surface is thus vitrified.

Samples 7, 10 & 15, have FeO quantities of less than 10 wt.% and SiO_2 contents greater than 68 wt.%. The measured values for aluminum oxide (Al_2O_3) are also somewhat higher in samples 7, 10 and 15 (>6.5 wt.%) compared to the other samples (<4 wt.%) (Figure 16).

Samples 7 & 10 are probably fragments of a smithing slag cake from the bottom of the blacksmith's hearth. This type of slag, from smithing, generally, forms at the bottom of the hearth, in the ash bed just below the tuyere. It has a hemispheric roundish or oval form. The bottom side is thus often convex. In European contexts, these cakes are often referred to as "PCBs" or plano-convex buns. The upper surface can be flat or slightly concave. Sometimes remains and traces of the refractory hearth lining can be visible on the lateral side (Pleiner, 2006, p.113). Unfortunately, the fragmental state of our samples cannot confirm their initial shape. But as explained above, the very low quantity of manganese which in these slags is only 0.1 and 0.7 wt.% (Table 1), is an indication to of their being part of the smithing process. In addition, in contrary to smelting slags, these slags are mainly composed of silicates in the form of cristobalite and quartz (68-77 wt.% of SiO_2 and only 4-9 wt.% FeO). Silicate components in smithing slags can be result of

contribution of the lining (hearth's wall) or originate from a sand flux, added onto the surface of the red-hot metal as an anti-oxidant, to avoid oxidizing the iron. This also helps to dissolve hammer-scale on the surface of the heated iron (Serneels, 1993, p.240). These are evidences which let us to classify these slags as smithing hearth bottom slags. Their vitreous glassy upper part corresponds to the melted flux. The non-melted grains of flux, as fine quartz filter downwards to join the bottom of the hearth with other sandy-clayey particles. The importance of this vitreous matrix is that it can signify that a high amount of an anti-oxidant is added during the process which is a characteristic of elaboration, repairing, or welding. On the other hand, the low concentration of iron oxides in the slag means that the workpiece has lost little iron during forging, which supports the hypothesis for the advanced stage of the forging process.

The small, microscopic fayalite domains between vitreous and siliceous zones in these samples can be part of smelting slags included in the bloom or ingot in the previous step which filtered down into the hearth by smithing hammering. They can also be result of long working process where iron oxides had time to grow up as laths of fayalite.

The presence of several peculiar rectangular shapes of iron oxides in samples 7 and 10 should not go unmentioned, which could indicate the remains of hammer-scales in an advanced stage of oxidation (Figure 9, f). Hammer-scales that filtered down in the hearth can be present in smithing slags in different states, from a metallic iron crust identical to the original hammer-scale to magnetite or even total fusion with an agglomeration of wüstite globules (Le Carlier, Leroy and Merluzzo, 2007, p.27).

In addition, plotting the samples on the $FeO+Al_2O_3+SiO_2$ phase diagram (Muan, 1957; Verein Deutscher Eisenhüttenleute, 1981) (Figure 18) demonstrates a clear distinction between the smelting and smithing slags and the furnace wall fragment, based on their chemical composition and working temperature. In this regard, the working temperature of the smithing slags (samples 7 & 10) has been higher than in the smelting slags.

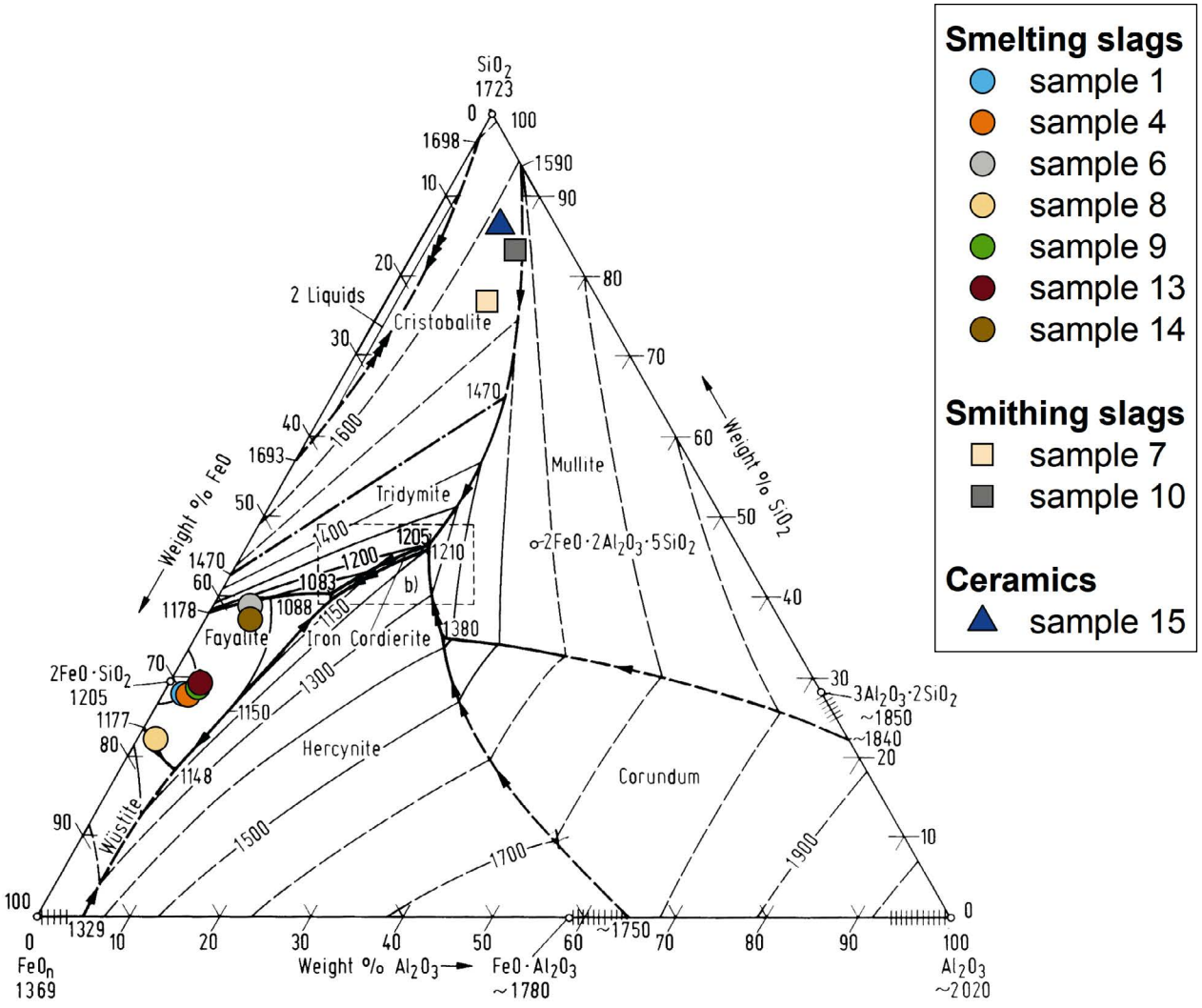

Figure 18. Representation of the FeO_n-Al_2O_3-SiO_2 system in equilibrium with iron according to Muan (1957) and Verein Deutscher Eisenhüttenleute (1981), sorted by find type.

Conclusion

Although we are aware of the similarity between copper and iron slags both in terms of their chemical composition and their mineralogical phases (Hauptmann, 2020, p. 368), the combination of macroscopic and microscopic observations and trace elemental analyses lead us to associate samples within this study to iron production.

The chemical comparison of the samples with regard to the most important elements for slag formation shows that the smelting slags can be differentiated from smithing slags and ceramics. Their high percentage of manganese (4.9 to 8 wt.%) parallels FeO contents of between 37 and 56 wt.% which are typical of smelting slags from the bloomery process. The same applies to SiO_2 with values between 26 and 35 wt.% (Pleiner, 2000, pp.251-255; Serneels, 1993). In contrast, smithing slags contain 4.8-9.3 wt.% FeO, 68.4-77.1 wt.% SiO_2, and 0.12-0.77 wt.% MnO. Such low iron and high quartz values in smithing slags may be due to the fact that quartz was added in the process. This happens, for example, during welding when a lot of flux is needed to prevent the iron from oxidizing (Pleiner, 2006, pp.109-112). The high percentage of manganese, in the smelting slags indicates that manganese rich iron ores were utilized. There are several iron-manganese-deposits in western Iran (Ghorbani, 2008): ShamsAbad deposit in Markazi Province (Fe, Mn, Pb, Zn, Ag, Cu including limonite, goethite, hematite, and pyrolusite), Khugan-Songol deposit (Fe, Pb, Ag, Ba), Ahangaran deposit (Fe, Pb, Zn, Ag, Au, Cu, Ba, Mn) and Malayer Mn-Fe deposit in Hamedan Province (Limonite and hematite; 30-49 % Fe and 3.3-4.8 % Mn) are among the known iron deposits at a distance around 100-150 km from the sites of this study (Figure 1). Farther away, toward the north and northeast, other deposits have also been reported at Galali/Hamekasi (magnetite, hematite), Deh Khazal (hematite), BabaAli (epidote, amphibole, garnet, and magnetite), Deh Hosein (Cu-Sn-As-Pb-Bi-W-Fe), and Nezam Abad (W-Cu-Sn) (Momenzadeh, 2004; Nezafati, 2006; Nezafati, Pernicka and Momenzadeh, 2009; Nabatian, et al., 2015, Fig.12). Traces of ancient (possibly iron) mining have been attested at least from the Ahangaran mine, which literally means blacksmiths' mine, (Momenzadeh, et al., 1979). We should also keep in mind that some of these ore bodies could have been worked not necessarily for iron but for other metals in ancient times (e.g. Deh Hosein and Nezam Abad). In addition to these registered deposits, closer to our region, Mehrab Kuh, north-west of Dorud, Khorramabad, Mamulan, Haft Cheshmeh, and Kuh Dasht (magnetite, hematite and pyrite) are other potential iron rich areas, although not yet with known traces of any mining (Emami, Elikay Dehno and Geravand, 2017, p.91) (Figure 1).

High manganese contents in iron ore also favors iron extraction during smelting. Like fayalite (Fe_2SiO_4), tephroite (Mn_2SiO_4) belongs to the olivine group of minerals. Both have been detected microscopically in the smelting slags (see above). As manganese is not reduced in the bloomery process and passes into the slag, it replaces iron in the formation of olivine, which can improve the iron yield.

As we have a very limited number of samples per site, we are unable to present a definite opinion concerning the production process.

For the moment, what is evident is that among the five sites, Sar Merang has the highest concentration of slags, as in other sites slags are more scattered. As slags can be transported and reused, we keep the possibility in mind that these sites may have not been the direct place of metalworking activity, even if they show that the activities occurred nearby.

Smelting slags are attested in all our five sites, although, smithing slags are only attested in Sar Merang. Based on geochemical, mineralogical, and lead isotopic investigations, the metallurgical processes in Cheshmeh Saleh (representing by sample 1) and Seyl Jengir (representing by sample 14) suggest partial similarities in terms of ore resources and working technologies.

The similarity between the chemical characteristics of smithing slags from Sar Merang (samples 7 & 10) and wall fragments of the furnace lining from Seyl Jengir (sample 15) may indicate the use of similar clay for the construction of the furnace. These two sites, about 38 km apart and located in a similar geological formation, probably had access to the same clay for the construction of the furnace. We have not further investigated the question of the origin of the furnace material. From the similarity of the geological formations alone, we can conclude that the soil used was the same. We prefer not to discuss this question further at this point, as it would require far more samples and research into the clay used to make furnaces.

Presence of both smelting and smithing slags in Sar Merang attests that people in this place had the knowledge for both processes. In this stage, it is not possible to know which process was their main activity. But the location of the site on the top of a plateau exposed to the wind may have provided favorable conditions for the setting up a smelting furnace. The presence of architectural structures and pottery sherds on the surface can lead to the hypothesis that we are not far from a settlement place. Workers used tools and tools need to be made and repaired. So, it's not surprising to find smithing activity

nearby or at smelting sites. Unfortunately, no charcoal was found among our samples. So, no C^{14} analysis could be undertaken.

Based on our studies, the Ahangaran mine could have partly provided the ore for the production of the slags at Cheshmeh Saleh and Seyl Jengir, while the ShamsAbad mine seems to be an anomaly. Although Deh Hosein and Nezam Abad mines isotopically match rather well with some of the slag samples, their geochemistry is incompatible with the slags. Anyhow, in order to obtain more information, it is immensely important to investigate the surrounding deposits chemically and isotopically. Even though this study contains only a few samples, the high manganese values combined with the lead isotopic subgroups are already good indications of what needs to be taken into account when searching for the ore deposits. In this regard, it seems that the central and northern part of the Sanandaj-Sirjan metallogenic zone of Iran could be a favorable area for further research.

Acknowledgments

This article is an output of Heinrich Winkelmann fellowship attributed to Zahra Hashemi in 2021-2022. The authors would especially like to thank Professor Dr. Thomas Stöllner for his support and the Deutsches Bergbau-Museum, Bochum, which funded the analytical costs. Dr. Michael Bode and Dr. Moritz Jansen, who carried out the elemental and lead isotope analysis are also thanked for their efforts. We would also like to thank the Iranian Ministry of Cultural Heritage and Handicrafts and especially Dr. Ata Hasanpour for their valuable support during the survey mission.

References

Connelly, G., Hartshorn, R.M., Novozymes, T. D. and Hutton, A.T. eds., 2005. *Nomenclature of Inorganic Chemistry.* International Union of Pure and Applied Chemistry IUPAC Recommendations 2005. Issued by the Division of Chemical Nomenclature and Structure Representation in collaboration with the Division of Inorganic Chemistry, IUPAC Red Book, RSC Publishing. Norfolk: Biddles Ltd, King's Lynn, UK.

Contenau, G. and Ghirshman, R., 1935. *Fouilles du Tepe Giyan, près de Nehavand, 1931 et 1932.* Paris: Musée du Louvre, Département des Antiquités.

Degryse, P., Schneider, J., Kellens, N., Waelkens, M., and Muchez, P.M., 2007. Tracing the resources of iron working at ancient Sagalassos (south-west Turkey): A combined lead and strontium isotope study on iron artefacts and ores. *Archaeometry*, 49(1), pp.75-86.

Ehya, F. and Marbouti, Z., 2021. The Shamsabad Fe-Mn deposit, Markazi province, Iran: LA-ICP-MS and sulfur isotopic geochemistry. *Ore Geology Reviews*, 104555. https://doi.org/10.1016/j.oregeorev.2021.104555.

Elikay Dehno, S., Akbari, T., Garavand, M., Rostami Charati, F. and Rahimi, F., 2022. Metallurgical Studies on Samples from Central Zagros, Northern Kuhdasht. *Journal of Anthropological Archaeology*, 2, pp.81-91.

Emami, M.A., Elikay Dehno, S. and Geravand, M., 2017. Ancient Metalworking in Southern Kuhdasht County: A Study of Smelting Slag from Botkhaneh Cave. *International Journal of the Society of Iranian Archaeologists,* 3(6). pp.100-109.

Erb-Satullo, N.L., 2019. The innovation and adoption of iron in the ancient Near East. *Journal of Archaeological Research*, 27, pp.557-560.

France-Lanord, A., 1969. Le fer en Iran au premier millénaire avant Jesus Christ. *Revue d'histoire des mines and metallurgie*, I, pp.75-126.

Ghorbani, M., 2008. *Economic Geology of the Ore and Natural Resources of Iran.* Tehran, Iran: Arian Zamin Publication.

Goldschmidt, V., 1937. The principles of distribution of chemical elements in minerals and rocks. *Journal of the Chemical Society*, pp.655-673.

Haerinck, E. and Overlaet, B., 1998. *Chamahzi Mumah: An Iron Age III Graveyard.* Luristan Excavation Documents, 2, Acta Iranica, 33. Leuven: Peeters.

Haerinck, E. and Overlaet, B., 1999. *Djub-i Gauhar and Gul Khanan Murdah: Iron Age III Graveyards in the Aivan Plain.* Luristan Excavation Documents, 3, Acta Iranica, 36. Leuven: Peeters.

Haerinck, E., Overlaet, B., 2004. *The Iron Age III Graveyard at War Kabud, Pusht-i Kuh, Luristan.* Luristan Excavation Documents, 5, Acta Iranica, 42. Leuven: Peeters.

Hashemi, Z., Malekzadeh M. and Hasanpour, A., 2023. Sangtarashan: L'Âge du Fer au Pish Kuh du Luristan. In: B. Overlaet: *Acta Iranica*, 62. Leuven: Peeters.

Hauptmann, A., 2020. *Archaeometallurgy, Materials Science Aspects.* Cham: Springer.

Le Carlier C., Leroy, M. and Merluzzo, P., 2007. L'apport de l'analyse morphologique, microscopique et chimique des scories en forme de culot à la restitution des activités de forge. *Archeosciences*, 31, pp.23-35.

Maanijou, M., Tale Fazel, E., Hayati, S., Mohseni, H. and Vafaei, M., 2020. Geology, fluid inclusions, C–O–S–Pb isotopes and genesis of the Ahangaran Pb-Ag (Zn) deposit, Malayer-Esfahan Metallogenic Province, western Iran. *Journal of Asian Earth Sciences*, 195, 15 June 2020, 104339. https://doi.org/10.1016/j.jseaes.2020.104339.

McDonough, W.F. and Sun, S.S., 1995. The composition of the Earth. *Chemical Geology*, 120(3-4), pp.223-253. https://doi.org/10.1016/0009-2541(94)00140-4.

Milot, J., Poitrasson, F., Baron, S. and Coustures, M.P., 2016. Iron isotopes as a potential tool for ancient iron metals tracing. *Journal of Archaeological Science*, 76, pp.9-20.

Momenzadeh, M., Shafighi, S., Rastad, E. and Amstutz, G.C., 1979. The Ahangaran lead-silver deposit, SE Malayer, west central Iran. *Mineralium Deposita*, 14, pp.323-341.

Momenzadeh, M., 2004. Metallic mineral resources of Iran, mined in ancient times: a brief review. In: T. Stöllner, R., Slotta and A., Vatandoust, eds. 2004. *Persiens Antike Pracht. Bergbau - Handwerk - Archäologie. Katalog der Ausstellung des Deutschen Bergbau-Museums Bochum vom 28. November 2004 bis 29. Mai 2005. Band 1. Veröffentlichung aus dem Deutschen Bergbaumuseum,* Nr. 128. Bochum: Deutsches Bergbau-Museum Bochum. pp.8-21.

Muan, A., 1957. Phase equilibria at liquidus temperatures in the system iron oxide Al2O3-SiO2 (subscripts?) in air atmosphere. *Journal of the American Ceramic Society*, 40, pp.121-133.

Nabatian, G., Rastad, E., Neubauer, F., Honarmand, M. and Ghaderi, M., 2015. Iron and Fe–Mn mineralisation in Iran: implications for Tethyan metallogeny. *Australian Journal of Earth Sciences,* 62, pp.211-241.

Nezafati, N., 2006. *Au-Sn-W-Cu-Mineralization in the Astaneh-Sarband Area, West Central Iran: including a comparison of the ores with ancient bronze artifacts from Western Asia.* Ph. D. University of Tübingen. Online available at: https://publikationen.uni-tuebingen.de/xmlui/handle/10900/48972 [Accessed 08.01.2024].

Nezafati, N., Pernicka, E. and Momenzadeh, M. 2009. Deh Hosein; an ancient tin-copper mine in western Iran. *Annual Journal of Archaeology, the Turkish Academy of Sciences -TÜBA-AR,* 12, pp 223-236.

Overlaet, B., 2003. *The Early Iron Age in the Pusht-i Kuh, Luristan.* Luristan Excavation Documents 4, Acta Iranica 40. Leuven: Peeters.

Pigott, V.C., 1989. The Emergence of Iron Use at Hasanlu. *Expedition Magazine,* 31(2-3), pp.67-79.

Pleiner, R., 2000. *Iron in Archaeology: The European Bloomery Smelters*. Archeologický ústav AVČR. Praha.

Pleiner, R., 2006. *Iron in Archaeology: Early European Blacksmiths.* Archeologický ústav AVČR. Praha.

Rehder, J.E., 1991. The decorated iron swords from Luristan: Their material and manufacture. *Iran*, 29, pp.13-19.

Serneels, V., 1993. *Archéométrie des scories de fer, Recherches sur la siderurgie ancienne en Suisse occidentale. Lausanne :* Cahiers d'Archéologie Romande.

Schmidt, E.F., Van Loon, M.N., Curvers, H.H., 1989. *The Holmes Expeditions to Luristan*. The University of Chicago Oriental Institute Publications 108. Chicago: Oriental Institute of the University of Chicago.

Schwab, R., Heger, D., Höppner B. and Pernicka, E. 2006. The provenance of iron artefacts from Manching: A multi-technique approach. *Archaeometry*, 48(3), pp.433-452.

Smith, C.S., 1971. The techniques of the Luristan smith. In: R.H. Brill, ed. 1971. *Science and Archaeology.* Cambridge: MIT Press. pp.32-54.

Stepanov, S., Lloyd Weeks, L., A. Franke, K., Overlaet. B., Alard, O., Charlotte Cable, C.M., Yousif Al Aali, Y., Boraik, M., Zein, H. and Grave, P., 2020. The provenance of early Iron Age ferrous remains from southeastern Arabia. *Journal of Archaeological Science*, 120, pp.1-21.

Taylor, R.N., Ishizuka, O., Michalik, A., Miltona, J.A., and Croudacea, I.W., 2015. Evaluating the precision of Pb isotope measurement by mass spectrometry. *Journal of Analytical Atomic Spectrometry, Royal Society of Chemistry,* 1. [online] Available at: <https://pubs.rsc.org/en/content/articlelanding/2015/ja/c4ja00279b> [Accessed 22 August 2024].

Verein Deutscher Eisenhüttenleute, 1981. *Schlackenatlas.* Düsseldorf: Verlag Stahleisen.

Zamanian, H. and Radmard, K., 2016. Geochemistry of the rare earth elements in the Baba Ali magnetite skarn deposit, western Iran-A key to determine the conditions of mineralization. *Geologos*, 22(1), pp.33-47.

Zhan, Y.X, Xiao-Chun Li, X.C, Wu, B., Yang, K.F., Fan, H.R. and Li, X.H., 2023. The occurrence and genesis of HREE-rich minerals from the giant Bayan Obo deposit, China. *Ore Geology Reviews*, 157, 105438. https://doi.org/10.1016/j.oregeorev.2023.105438.

Authors

Zahra Hashemi (Corresponding author)
Department of Oriental Antiquities
Louvre Museum
Pavillon Mollien
75001 Paris, France
zahra.hashemi@louvre.fr
ORCID 0000-0002-5236-8945

Nima Nezafati
Deutsches Bergbau-Museum Bochum
Department of archaeometallurgy
Am Bergbaumuseum 31
44791 Bochum, Germany
nima.nezafati@bergbaumuseum.de
ORCID 0000-0002-5806-343X

Daniel Demant
Deutsches Bergbau-Museum Bochum
Department of mining archaeology
Am Bergbaumuseum 31
44791 Bochum, Germany
daniel.demant@bergbaumuseum.de
ORCID 0009-0004-6387-6867